AFRL-RV-PS-TR-2019-0022

AFRL-RV-PS-TR-2019-0022

ATOMIC-AND DEVICE-SCALE PHYSICS OF ION-TRANSPORT MEMRISTORS

Arthur H. Edwards

Air Force Research Laboratory
Space Vehicles Directorate
3550 Aberdeen Ave., SE
Kirtland AFB, NM 87117-5776

13 June 2019

Final Report

APPROVED FOR PUBLIC RELEASE; DISTRIBUTION IS UNLIMITED.

AIR FORCE RESEARCH LABORATORY
Space Vehicles Directorate
3550 Aberdeen Ave SE
AIR FORCE MATERIEL COMMAND
KIRTLAND AIR FORCE BASE, NM 87117-5776

DTIC COPY

NOTICE AND SIGNATURE PAGE

This report is the result of contracted fundamental research which is exempt from public affairs security and policy review in accordance with AFI 61-201, paragraph 2.3.5.1. This report is available to the general public, including foreign nationals. Copies may be obtained from the Defense Technical Information Center (DTIC) (http://www.dtic.mil).

AFRL-RV-PS-TR-2019-0022 HAS BEEN REVIEWED AND IS APPROVED FOR PUBLICATION IN ACCORDANCE WITH ASSIGNED DISTRIBUTION STATEMENT.

//signed//

ARTHUR EDWARDS
Program Manager

//signed//

DAVID WILT
Tech Advisor, Space Component Technology Branch (Acting)

//signed//

JOHN BEAUCHEMIN
Chief Engineer, Spacecraft Technology Division
Space Vehicles Directorate

REPORT DOCUMENTATION PAGE

Form Approved
OMB No. 0704-0188

1. REPORT DATE *(DD-MM-YYYY)* 28-04-2019	**2. REPORT TYPE** Final Report	**3. DATES COVERED** *(From - To)* 01 Oct 2014 – 28 Apr 2019

4. TITLE AND SUBTITLE
Atomic-and Device-Scale Physics of Ion-Transport Memristors

5a. CONTRACT NUMBER
In-House V0XQ

5b. GRANT NUMBER

5c. PROGRAM ELEMENT NUMBER
62601F

6. AUTHOR(S)
Arthur H. Edwards

5d. PROJECT NUMBER

5e. TASK NUMBER
PPM00015224

5f. WORK UNIT NUMBER
EF126580

7. PERFORMING ORGANIZATION NAME(S) AND ADDRESS(ES)
Air Force Research Laboratory
Space Vehicles Directorate
3550 Aberdeen Ave., SE
Kirtland AFB, NM 87117-5776

8. PERFORMING ORGANIZATION REPORT NUMBER

9. SPONSORING / MONITORING AGENCY NAME(S) AND ADDRESS(ES)
Air Force Research Laboratory
Space Vehicles Directorate
3550 Aberdeen Ave., SE
Kirtland AFB, NM 87117-5776

10. SPONSOR/MONITOR’S ACRONYM(S)
AFRL/RVSV

11. SPONSOR/MONITOR’S REPORT NUMBER(S)
AFRL-RV-PS-TR-2019-0022

12. DISTRIBUTION / AVAILABILITY STATEMENT
Approved for public release; distribution is unlimited.

13. SUPPLEMENTARY NOTES

14. ABSTRACT

We report on our key advances in understanding the physics of chalcogenide- and silicon dioxide-based conductive bridge random-access memory (CBRAM) devices. Specifically, we report on Ag and Sn in Ge2Se3 and in GeSe2, and Ag and Cu in SiO2. We report that Ag and Sn autoionize in Ge2Se3, but not in SiO2. This crucial difference is reflected in the growth of dendrites in both materials. We also found that in Ge2Se3, Ag will readily displace Ge, forming a Ge-Ag dimer. Furthermore, two Ag atoms can form Ag dimers, displacing a pair of Ge atoms, and that this is an exothermic reaction. We have also studied the interaction of oxygen with pure Ge2Se3, and with Ag in the same material. Oxygen molecules will readily dissociate and form a variety of stable and metastable defects. The lowest energy defect is a Ge-O-Ge bridge, thus eliminating Ge-Ge dimers. We also found that oxygen did not readily attack Ge-Ag dimers.

15. SUBJECT TERMS
Ge2Se3; memristor; oxygen defects; oxygen transport

16. SECURITY CLASSIFICATION OF:			**17. LIMITATION OF ABSTRACT**	**18. NUMBER OF PAGES**	**19a. NAME OF RESPONSIBLE PERSON** Arthur H. Edwards
a. REPORT Unclassified	**b. ABSTRACT** Unclassified	**c. THIS PAGE** Unclassified	Unlimited	66	**19b. TELEPHONE NUMBER** *(include area code)*

Standard Form 298 (Rev. 8-98)
Prescribed by ANSI Std. 239.18

--- This Page Intentionally Left Blank ---

TABLE OF CONTENTS

Section **Page**

LIST OF FIGURES

LIST OF TABLES

ABSTRACT

We report on our key advances in understanding the physics of chalcogenide- and silicon dioxide-based conductive bridge random-access memory (CBRAM) devices. Specifically, we report on Ag and Sn in Ge_2Se_3 and in $GeSe_2$, and Ag and Cu in SiO_2. We report that Ag and Sn autoionize in Ge_2Se_3, but not in SiO_2. This crucial difference is reflected in the growth of dendrites in both materials. We also found that in Ge_2Se_3, Ag will readily displace Ge, forming a Ge-Ag dimer. Furthermore, two Ag atoms can form Ag dimers, displacing a pair of Ge atoms, and that this is an exothermic reaction. We have also studied the interaction of oxygen with pure Ge_2Se_3, and with Ag in the same material. Oxygen molecules will readily dissociate and form a variety of stable and metastable defects. The lowest energy defect is a Ge-O-Ge bridge, thus eliminating Ge-Ge dimers. We also found that oxygen did not readily attack Ge-Ag dimers.

1.0 SUMMARY

In this report, we review the principal findings of our in-house effort on the physics of ion-transport memristors. We focused on chalcognide-based conductive bridge random access memory (CBRAM) devices, especially Ge-Se compounds, and within those devices, we focused on silver as the principal ion. Using a variety of theoretical methods, including density functional theory (DFT), compact models, and kinetic Monte Carlo (KMC), we made the following discoveries:

- We found that excess electrons spontaneously self-trap, and that they prefer to self-trap in pairs. In so doing, they break Ge-Se bonds. This is consistent with Elliott's contention that photo-doping of Ge-Se compounds requires a front of negatively charged defects ahead of a front of positive silver ions that spontaneously pulls them further in a selenium rich layer.
- Independent of stoichiometry, we found that interstitial silver atoms spontaneously autoionize, dropping an electron into the conduction band of the material. This explains the persistent mobility of silver ions under the influence of an external field.
- In our initial studies of multiple silver atoms, we found that they prefer to form interstitial dimers
- We found that silver is a fast diffuser– that it can traverse a 50 Å film in tens of nanoseconds. Within a crystalline model there are hard and easy pathways for diffusion. The easy paths are along the surface of layers. The hard hops are between interstitial positions within layers.
- In Ge_2Se_3, we found that, thermodynamically, silver will readily replace germanium in the lattice, forming Ge-Ag dimers and isolated germanium interstitials. This is consistent with Campbell's hypothesis that Ge-Ge dimers are the initial sites for silver incorporation, and form the backbone for the formation of silver dendrites.
- In $GeSe_2$, we found that silver does not readily replace germanium in the lattice. This is a key difference between selenium rich compounds, such as $GeSe_2$, and Ge_2Se_3.
- We found that monomeric silver chains do not, even asymptotically, become metallic. However, any more complex chain structures are metallic. Furthermore, we agree with others that roughly 40 silver atoms are required before we predict metallic behavior in finite clusters. Thus, we do not expect that small clusters will alter dramatically the electric field distribution in memristive devices.

2.0 INTRODUCTION

2.1 Background

Memristors may hold the key to very low power, neuromorphic computation. Many memristor technologies offer variable, nonvolatile resistance, making obvious their potential as artificial synapses [7]. One promising set of technologies use germanium-selenium compounds through which silver or copper ions move under applied bias to either form or dissolve highly conductive metallic dendrites. The process is shown, in broad outline, in Fig. 1.

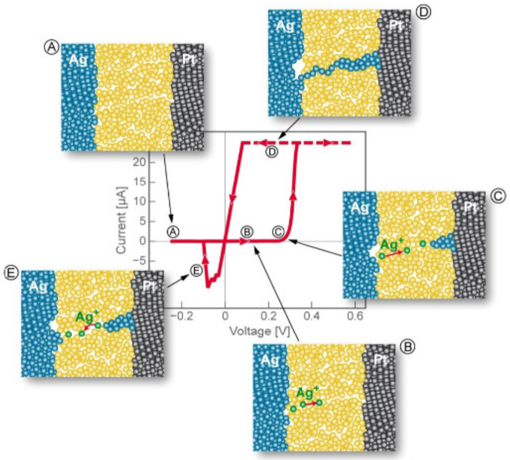

Figure 1: Memristor I-V curve and CBRAM diagrams. Yellow atoms indicate the electrolyte

Sub-figure marked A is the virgin device. The bottom electrode, in this case platinum, is inert, and serves as an ohmic contact. The yellow active layer can be an insulator, such as silicon dioxide, or an amorphous semiconductor, such as $GeSe_2$or Ge_2Se_3. The top electrode in this simple picture is a layer of silver, although a variety of metals have been shown to exhibit similar behavior. Under positive bias (B-D), silver atoms become positively charged, and transport rapidly through the active layer, finally depositing on the bottom electrode. As dendrites begin to form, they concentrate the electric field, so that dendrite growth is self-organized. The resistance of the device stays very high until the dendrite makes contact with the top electrode, at which point the resistance decrease is precipitous. In fact, the current is limited by specifying a compliance value. As the bias is reduced and becomes negative, the dendrite starts to lose silver ions to the top electrode, and , eventually, the connection is broken, driving the resistance back to a high value. Both high- and low-resistance states are stable at and below room temperature, so that the device is a variable, programmable resistor– a memristor. That the connection is dendritic, or filamentary, has been seen experimentally. In Fig. 2.

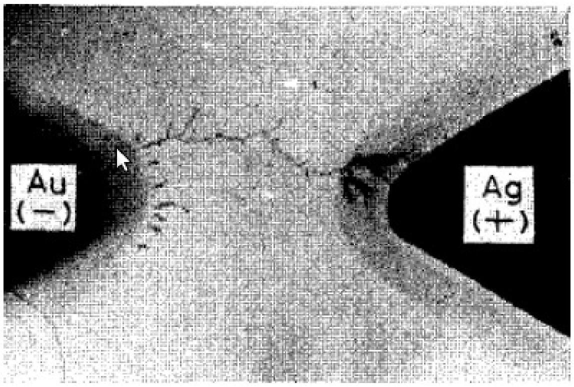

Figure 2: Micrograph of Ag dendrite between Ag and Au electrodes through As_2Se_3 [13]

We should point out that initially the large resistance change of up to three orders of magnitude led to hopes that these devices could be programmed into a very large number of intermediate states, leading to a new generation of nonvolatile, analog memories. However, the principal resistance range under control is after the dendrite has fully contacted the top electrode, and the range of variation is, at best, an order of magnitude. Furthermore, while several groups have demonstrated some analog behavior, the devices still exhibit larger device-to-device, and even intra-device, variation, so that the practical number of available states is in the low tens of states. Recently, Barnaby and coworkers have developed similar materials systems using amorphous silicon dioxide as the electrolyte [3, 4].

In this in-house effort, we have focused primarily, but not exclusively, on the Ge_2Se_3:Ag material system. We made this choice for several reasons. First, as discussed briefly below, there is a fairly large literature in selenium-rich materials, such as $GeSe_2$, so that we could make a much bigger impact on a new, technologically promising material. Second, it turns out that devices such as those shown in Fig. 1 need an initial photo-doping treatment that drives silver into the active layer, while devices that use Ge_2Se_3 require no such step. Third, the device technology using Ge_2Se_3 is more mature, leading to less device-to-device variability. Fourth, the Ge_2Se_3-technology has a much larger operating temperature range, able to meet military specifications. Finally, as discussed in Sec. 2.2.1, after photo-doping, the selenium-rich materials actually have many of the characteristics of Ge_2Se_3, including significant numbers of Ge-Ge dimers, so that understanding Ge_2Se_3 could well lead to broader understanding of Ge-Se-based devices. We will also report findings on the SiO_2:Ag and SiO_2:Cu systems. While devices based on the latter materials have similar characteristics, the basic physics is significantly different.

We undertook this study to build a fundamental knowledge-base for conductive bridge cells. Prior to the study, there was no clear understanding of how neutral silver or copper became positively charged, and how these ions transported through the solid. Even the required dimensions of dendrite to support metallic conduction were unknown. It was the goal of this effort to provide microscopic understanding of these and other crucial mechanisms. However, it is likely that real systems contain significant concentrations of various extrinsic species, including oxygen. Because of this possibility, we explored the interaction of oxygen atoms and molecules with Ge_2Se_3. We chose this because there is spectroscopic evidence that, even in selenium-rich compounds that require photo-doping, the backbone of the resulting alloy has a similar volume density of germanium dimers to Ge_2Se_3. The in-house results relied heavily on density functional theory (DFT) in the generalized gradient approximation (GGA). Using a crystalline model, we have calculated equilibrium geometries, defect levels, energies of formation, and core-level shifts for a variety of oxygen complexes, including interstitials, substitutionals, and complexes with silver using this model. We also performed limited studies of actual device performance using physics-based compact models, and even kinetic Monte-Carlo techniques [39]. We found that oxygen molecules either spontaneously dissociate, or they exist in highly metastable conformations. Thus, we only really need to study isolated oxygen atoms. We also find that, in the presence of germanium dimers, oxygen interstitials are unstable– that they form Ge-O-Ge bridges at room temperature. These results have implications for processing choices in Ge_xSe_y-based memristor technologies. The balance of the report is organized as follows: In Sec. 2.2, we review previous relevant experiment and theory on bulk Ge_2Se_3, and on oxygen in this system. In Sec. 3.0 we briefly review our methods, including the codes used in this study. The results are given in Sec. 4.0 , and we discuss future work in Sec. 5.0 .

2.2 Previous Experiment and Theory

2.2.1 Ge_2Se_3 Experiment

Ge_2Se_3 exists only in the non-crystalline state– when annealed, it phase-separates into $GeSe_2$, and GeSe. In the non-crystalline phase, Zhou, *et al.* [43] have shown that, on average, it follows the 8-N rule. That is, germanium is four-fold coordinated, with three selenium and one germanium nearest neighbors, while selenium is two-fold coordinated, with two germanium neighbors. This is consistent with the radial distribution function analysis of Pohle and coworkers, based on X-ray diffraction studies [32]. From optical absorption measurements, the energy gap, E_g, is somewhat controversial. Bakr *et al.* estimate the gap to be 2.0 eV [1]. Kotkata *et al.* quote values ranging from 1.36 eV to 1.62 eV, depending on the criteria [17]. In fact, depending on preparation technique, Choi shows a variation between 1.6 eV and 2.2 eV for the criterion that the absorption coefficient, α, is 10^{-4} cm^{-1}[5].

Yan, *et al.* have studied photobleaching in vacuum and in air for both $GeSe_2$ and Ge_3Se_2

[41]. They concluded that bond rearrangement was responsible for most of the photobleaching in $GeSe_2$ in both air and vacuum, while in Ge_2Se_3, it was almost exclusively due to oxygen incorporation, as there was no photobleaching observed from vacuum illumination.

The Raman spectra of various Ge-Se compounds, including Ge_2Se_3, as measured by Mitkova and Kozicki [24], is shown in Fig. 3.

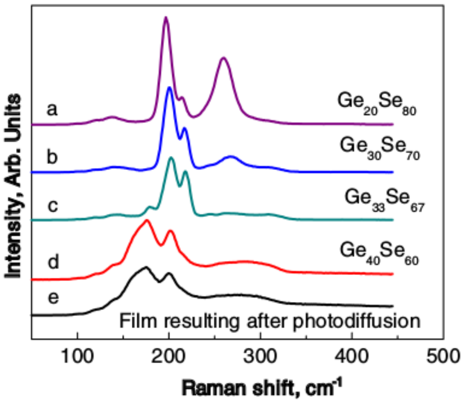

Figure 3: Raman spectra in GeSe compounds, before (a-d) and after (e) photodiffusion [24]

Note the crucial difference from the other, selenium-rich, films is a prominent feature at ˜180 cm^{-1}, associated with the stretching mode of Ge-Ge dimers, and the higher energy features associated with Ge-Se and Se-Se bonds. The Ge-Ge dimers are only abundant in the $Ge_{40}Se_{60}$ (Ge_2Se_3) compound. The curve labeled *e* is taken for each material after photodiffusion, where relatively high power, band gap light is used to drive elemental silver into the films. Note that after photo diffusion, all of the materials look the same as $Ge_{40}Se_{60}$. For this reason, we believe that the results obtained in this study will be relevant to other technologies.

2.2.2 Ge_2Se_3Theory

While there is a substantial literature on selenium-rich germanium-selenium compounds, including GeSe and $GeSe_2$ [11, 6, 22, 21, 43], there is relatively little published on Ge_2Se_3. Le Roux and co workers have published two quantum molecular dynamics studies– one on liquid Ge_2Se_3 [20], and one on glassy Ge-Se compounds, including Ge_2Se_3 [19]. The average coordination numbers for glassy Ge_2Se_3 are given in Ref. [19], which we reproduce in Table 1.

Table 1: Coordination numbers for QMD simulation of glassy Ge_2Se_3

$\bar{n}_{Ge}$	$\bar{n}_{Se}$	$\bar{n}$	$\bar{n}(exp)$	$\bar{n}(8-N)$
3.73	2.15	2.78	2.81	2.8

The *8-N* value is the ideal if all germanium atoms have four nearest-neighbors and all selenium atoms have two. While there is some deviation, the simulation is remarkably well ordered with respect to coordination numbers. However, the average number of Ge-Ge dimers/Ge atom is half of that expected from the EXAFS results of Zhou *et al.*[43]m and from assumed chemical ordering. It is not clear whether the QMD results are definitive. As an example, in SiO_2, we cite Ref. [14] that obtained excellent agreement with neutron diffraction studies, while retaining relatively large densities of structural defects, such as non-bridging oxygen atoms, that are absent in more recent simulations that either use better potentials [34, 38], or anneal more slowly. Until there are good force fields in classical MD for the Ge-Se interaction, the quality of the quantum MD results will be controversial.

3.0 METHODS

We used SEQQUEST, a pseudo potential DFT code, that uses well-converged, valence atomic orbital basis sets (double-zeta quality) that include polarization functions. We used Hamann-type, norm-conserving pseudo potentials [12], and the Perdew-Burke-Ernzerhoff (PBE) formulation [30] of the generalized gradient approximation (GGA). We used a 2x2x2 Monkhorst-Pack sampling of *k*-space [25]. Geometry relaxations are converged to within 0.01 eV/Å. We used a crystalline model based on Si_2Te_3, shown in Fig. 4.

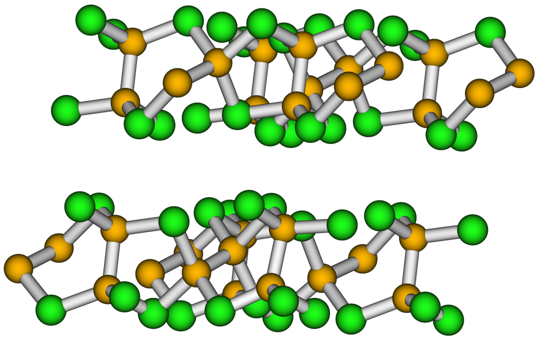

Figure 4: Crystalline model for Ge_2Se_3 [31]

This model retains the strict chemical ordering expected from the stoichiometry, which was observed in EXAFS, and reproduced, to a large extent, in MD simulation. Note that this is predicted to be a layered material, similar to crystalline $GeSe_2$. This is not surprising, as other crystalline chalcogenide materials, such as orthorhombic GeTe, $GeTe_2$, and $Ge_2Sb_2Te_5$, are also layered. Of course, in the actual amorphous state, there is no evidence for long-range layering in these materials. However, in a-$Ge_2Sb_2Te_5$ there is experimental evidence for large voids, that we argue is a remnant of frustrated layering. We should note that the germanium dimers are of two types– either approximately parallel or perpendicular to the layer surface. The two have surprisingly different geometries, the bond lengths differ by 0.1 Å, and, as shown in Sec. 4.0 and elsewhere [8], different reaction energetics. We use $D_\perp$ and $D_\parallel$ to distinguish the two conformations. The results reported here will be useful to understand the chemistry in chemically ordered portions of an amorphous phase. However, they will not have relevance for over- and under- coordinated species. Furthermore, we expect inhomogeneous broadening due to local strain, so results reported here are incomplete. None of the structures reported here have associated localized states within the Kohn-Sham band gap, so, for chemically ordered Ge_2Se_3, we predict there will be no defect levels in the band gap.

For extrinsic defects, we used 80 and 360 atom supercells to test convergence. We have studied single and paired metal atoms (Ag, Sn, Cu) and oxygen. For the metal atoms, we have studied charge-states, although, as shown in Sect. 4.0 , this is complicated by self-trapping we discovered. For self-trapping, and for the emergence of conduction, we used clusters of atoms. For self-trapping, we used the cluster shown in Fig. 5.

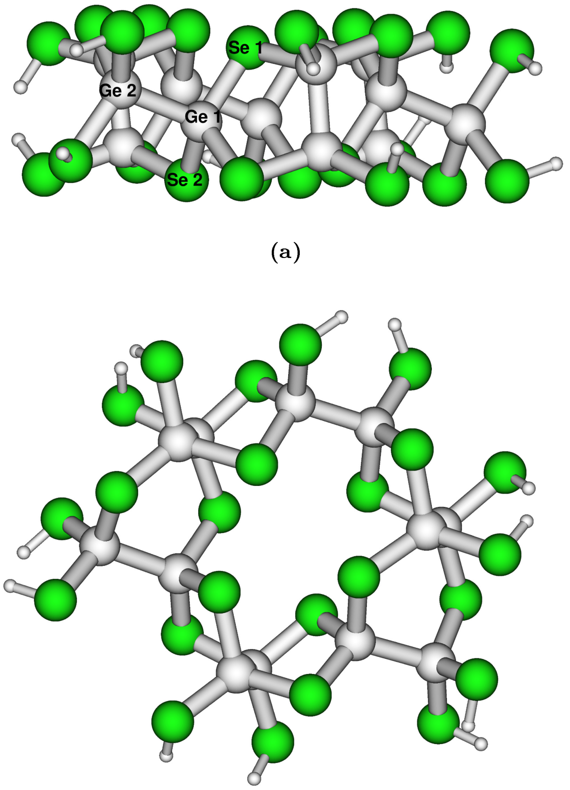

(a)

(b)

Figure 5: Two views of the cluster used for self-trapping study: Small spheres are hydrogen atoms

We abstracted a ring-structure from the larger super cell, truncated on selenium atoms because of their low coordination number. The dangling selenium orbitals were saturated with hydrogen atoms at the equilibrium Se-H bond length, and along the bond directions in the original cell. We chose this structure because there is no single preferred site in the cluster, so that we could make sensible arguments about transport of self-trapped species. For onset of conduction, we used clusters of silver atoms of various sizes and shapes. We used GAMESS for the cluster calculations, and used configuration interaction (singles) to calculate first excited states. We performed one-dimensionally periodic calculations on linear chains of varying thickness using QUEST, again using the PBE ECP.

As part of an initial effort to model devices using results from atomistic simulations, we wrote a kinetic Monte Carlo code, based on Ref. [39]. The Kinetic Monte Carlo (KMC) is an excellent technique for bridging atomistic and nanometric length scales. It builds a probabilistically weighted list of possible reactions, and then chooses reactions base on a uniformly distributed random number. The time step is variable, and depends on this stochastically chosen process. Thus, KMC can span large time intervals using mechanisms based on atomistic simulations.

4.0 RESULTS

4.1 Ge_2Se_3

4.1.1 Crystalline Model

In Table 2, we summarize our local geometric predictions from the crystalline model, and compare these with the EXAFS results of Zhou *et al.* [43], and to molecular dynamics (MD) of Leroux *et al.* [19].

Table 2: Bond lengths for crystalline model of Ge_2Se_3, EXAF's [43], and MD [19]

	R_{Ge-Ge} (Å)	R_{Ge-Se} (Å)
Current Study	2.45±0.05	2.41±0.02
Ref. [19]	2.47	2.35
Ref. [43]	2.41±0.02	2.365±0.005

For both bond lengths, our results are approximately 1.7% larger than the experimental values. Note also that our standard deviation of bond lengths across the twenty atom unit cell is between two and four times larger than experiment. This is a little surprising, considering that experiment is actually over a truly amorphous material. We have also included results from the radial distribution functions for Ge-Ge and Ge-Se bonds from Ref. [19]. Two features bear noting. First, the Ge-Ge bond lengths predicted in the current study, and by Le Roux and coworkers, are significantly larger than that obtained from EXAFS by Zhou and coworkers. More importantly, the bond statistics in the molecular dynamics study are significantly less ideal than those reported in EXAFS. That is, while the EXAFS data indicates perfect chemical ordering, within experimental error, with, on average, one germanium and three selenium neighbors for each germanium atom, and two germanium neighbors for each selenium atom, the molecular dynamics study indicates only one in two germanium atoms with a germanium neighbor. If the experiment is to be believed, this discrepancy may indicate poor convergence due to an overly aggressive annealing schedule. At any rate, we argue that the results for the crystalline model reflect faithfully the local chemical bonding, so that the predicted local chemistry will reflect what is seen in well annealed, bulk glass. One final note on the two dimer conformations $D_{\parallel}$ and $D_{\perp}$. The two conformations have bond lengths that differ by 0.1 Å ($D_{\perp} < D_{\parallel}$), which is reflected in the projected density of states (PDOS), shown in Fig. 6 where the lowest peak in the conduction band is from $D_{\parallel}$ (Ge_1), and the second is from $D_{\perp}$ (Ge_2).

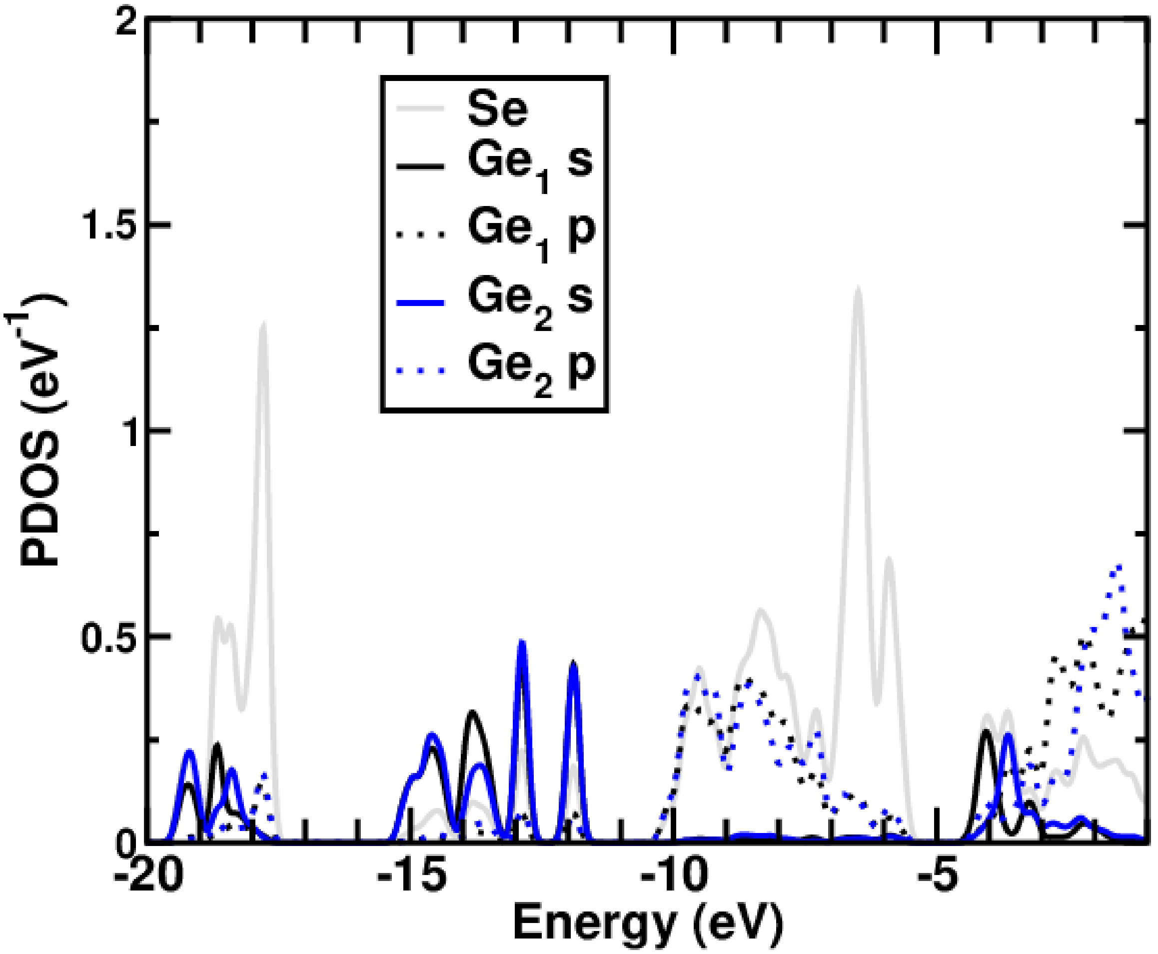

Figure 6: PDOS of two germanium atoms in the ideal crystalline model: Ge_1(Ge_2) part of $D_{\parallel}$($D_{\perp}$)

Normally, one would argue that the smaller bond length implies stronger bonding. However, the positions of the selenium atoms above and below $D_\perp$ are partly determined by the Ge-Se bond lengths surrounding $D_\parallel$, so that the smaller $D_\perp$bond length could imply strain induced by geometric constraints. We include this discussion, as it pertains to oxygen interactions in Sec. 4.3.

4.1.2 Electron self-trapping

Prior to discussing extrinsic defects, or even structural, intrinsic defects, such as vacancies, antisites, or interstitials, there is great interest in chalcognide materials, such as $GeTe_2$, $GeSe_2$, and Ge_2Se_3 in the self-trapping of electrons and holes. In fact, these are the model materials for self-trapping. We have performed *ab initio* and nearly *ab initio* calculations using density functional theory (DFT) applied to either periodic unit cells, or finite atomic clusters, shown in Figs . 4 and 5. We derive both from a crystalline model based on Si_2Te_3 [31]. We include the top view, Fig. 5 (b), to show clearly the larger and smaller ring structure. To reiterate, for the periodic structures, we used SEQQUEST, a local orbital, pseudo potential, DFT code. We used the generalized gradient approximation (GGA), the Perdew-Burke-Ernzerhof (PBE) exchange-correlation potential [30], and Hamann pseudopotentials [12]. For the cluster calculations, we combined SEQQUEST with GAMESS [35], an atomic and molecular code, where we used Stevens-Basch-Krauss effective core potentials[36, 40] and basis sets, combined with either the Becke 3 parameter Lee Yang Parr (B3LYP) [2] or the PBE exchange correlation potentials. For atomic relaxations, we used two sets of boundary conditions. Either we allowed all atoms, including the hydrogen atoms, to relax, or we froze the terminating Se-H moieties and allowed all interior atoms to relax. We label these unconstrained, *u,* and constrained, *c*, respectively. Clearly, the freedom of the real relaxation is between these two extremes, so commonality will be an important metric of validity. Another important metric will be the degree to which self-trapping occurs on the interior, heavy atoms. Hydrogen contamination of the trapped electron wave function would result if the LUMO had significant hydrogen content– an artifact that would invalidate any predictions for pure Ge_2Se_3. We calculated equilibrium geometries, and stabilization energies in the neutral, -1 and -2 charge states. In the -1 charge state, there is an unpaired spin that would give rise to a measurable electron spin resonance (ESR) signal, along with hyperfine structure. Using NWChem [37], we calculated the isotropic and anisotropic hyperfine coupling constants for ^{73}Ge and ^{77}Se with the all-electron, double-zeta plus polarization (DZP) basis set optimized for B3LYP [33]. We calculated the barrier to hopping using the nudged elastic band (NEB) technique [16] in SEQQUEST. This required the location of metastable local minima. As described below, we started from a geometry analogous to the ground state, but translated the localizing distortion to neighboring atoms, and searched for local minima. In SEQQUEST, the cluster calculations are performed in a repeated cell approximation. Because the basis sets and pseudopotentials in SEQQUEST are different from those used in GAMESS, prior to calculating the barrier, we recalculated local minimum energy configurations. Because SEQQUEST performs DFT calculations only in the local density approximation (LDA), and the PBE, and Armiento-Mattsson (AM05) versions of GGA, albeit in both restricted and spin-polarized formalisms, and because PBE is known to underestimate barrier heights [27], sometimes dramatically, we estimated B3LYP barrier heights using the PBE conformations for the ground and transition states. We used the B3LYP barriers to make contact with experiment.

In Figs. 7 (a) and (b) we show the relaxed constrained cluster in the -1 and -2 charge states, respectively.

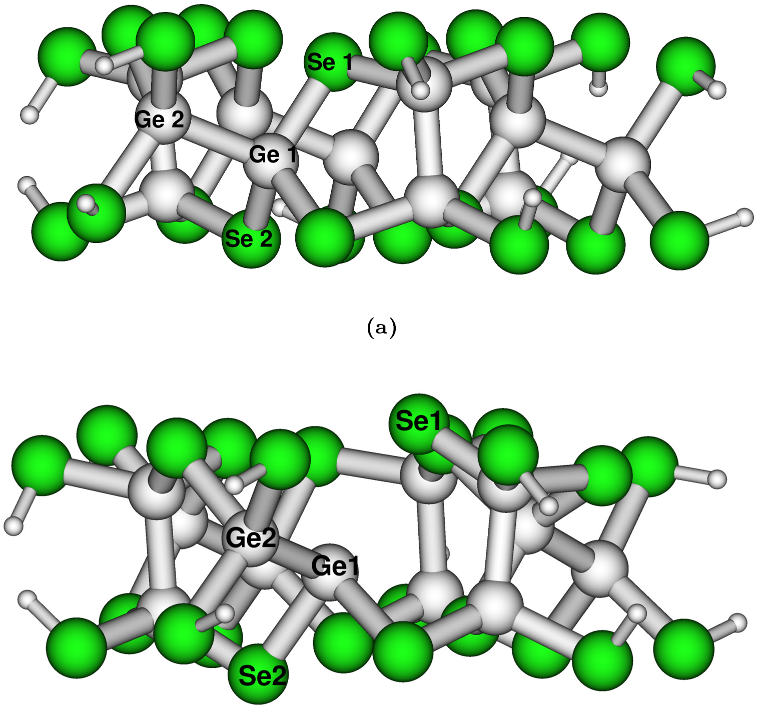

(a)

(b)

Figure 7: B3LYP constrained geometries in the (a) -1 , and (b) -2 charge state

Table 3 summarizes the important changes between the neutral, -1, and -2 charge states as a function of exchange-correlation potential and cluster constraints. We have not included the unconstrained parameters for the -2 charge state because we deemed it unphysical. More on this below. Aside from the numbered pair of germanium atoms in Fig. 7 and their nearest neighbor selenium atoms, relaxations are negligible between charge states. However, within that moiety, electron trapping leads to large atomic relaxations. In fact, in the -2 charge state, the bond ruptures between Ge_1 and Se_1. Independent of geometrical constraints, the trapping event consists in a lengthening of one Ge-Ge bond and two Ge-Se bonds. The unconstrained results are especially important for assessing the degree to which the electron is trapped in the interior of the cluster. From Table 3, both the direction and the length of the Se-H bonds are essentially unchanged by the presence of one extra electron. Furthermore, in this equilibrium configuration, the electron clearly traps on an interior selenium atom bound to two germanium atoms. Finally, in Table 4 we show the energy difference in the -1 and -2 charge states between the neutral equilibrium and the localized conformations. This is an estimate of the self-trapping energy and does not include the long-range polarization energy that would increase the stability further.

Table 3: (a) Geometric parameters. c (u)= constrained (unconstrained) clusters. Numbering from Fig. 7 o ,-,= neutral -1e, -2e . For cluster results, values outside (inside) parentheses are for PBE (B3LYP) (b) Analogous results for the periodic supercell calculation: column headers indicate charge state

(a)

	u^o	c^o	u^-	c^-	$c^=$
$R_{Ge_1-Ge_2}$ (Å)	2.51 (2.51)	2.52 (2.51)	2.58 (2.58)	2.60 (2.60)	2.72 (2.74)
$R_{Ge_1-Se_1}$ (Å)	2.46 (2.45)	2.45 (2.45)	2.74 (2.78)	2.64 (2.69)	3.54 (3.46)
$R_{Ge_1-Se_2}$ (Å)	2.43 (2.43)	2.45 (2.45)	2.59 (2.62)	2.62 (2.65)	2.58 (2.62)
$<R_{Se-H}>$ (Å)	1.50 (1.49)	1.46 (1.46)	1.50 (1.49)	1.46 (1.46)	1.46 (1.46)
$\angle Ge_2 - Ge_1 - Se_1$	97.3 (99.2)	102.8 (102.7)	93.7 (93.6)	99.0 (98.1)	103.8 (96.3)
$\angle Se_2 - Ge_1 - Se_1$	112.7 (112.8)	(119.4)	153.5 (154.9)	138.9 (138.7)	152.7 (154.4)

(b)

	0	-1	-2
$R_{Ge_1-Ge_2}$	2.49	2.50	2.59
$R_{Ge_1-Se_1}$	2.42	2.43	2.93
$R_{Ge_1-Se_2}$	2.43	2.44	2.61
$\angle Ge_2 - Ge_1 - Se_1$	103.9	103.9	97.4
$\angle Se_2 - Ge_1 - Se_1$	117.6	103.9	158.7

Table 4: Approximate stabilization energy, in eV, for the single and paired self-trapped electron

	u^-	c^-	$c^=$
B3LYP	1.55	0.4	1.39
PBE	0.56	0.32	0.8

Clearly, the localized conformation is the ground state of this system. As expected, the unconstrained cluster has a much larger stabilization. Also, B3LYP predicts a much larger stabilization energy. More importantly, we note that the stabilization energy for the -2 charge state is larger than twice the stabilizaton energy of the -1 charge state. This implies that, in the ground state, STE's would spontaneously pair.

The supercell results are summarized in Table 3 (b). In the -1 charge state, the electron is completely delocalized, and, there is virtually no difference in geometry between the neutral and the negative charge state. To eliminate the possibility that there was a barrier to self-trapping in the bulk, we used initial geometries taken from the relaxed cluster calculations. The supercell always relaxed back into the undistorted conformation. This was expected, as DFT has historically either missed self-trapping entirely, or has captured it as a metastable state. However, in the -2 charge state, there is clear evidence of self-trapping. The geometry is in very good agreement with the constrained cluster result, and justifies neglecting the unconstrained cluster result for this charge state. This is shown graphically in Fig. 8.

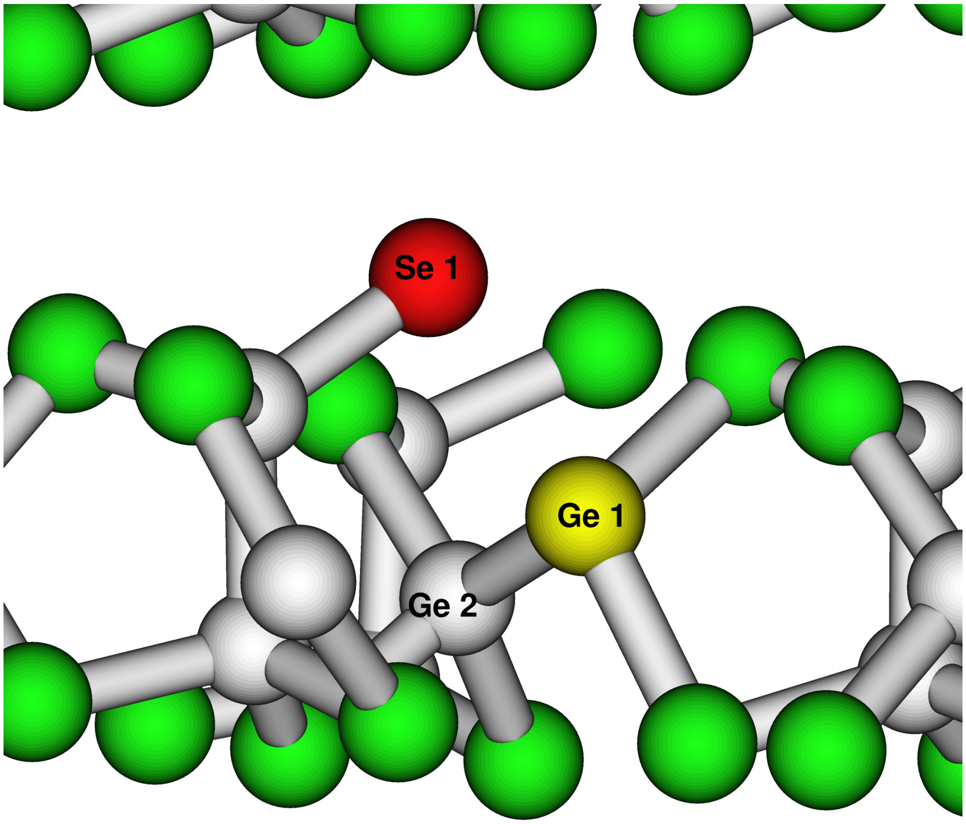

Figure 8: Geometry of the -2 charge state in the periodic calculation

Another important measure of localization is the appearance of one-electron levels in the Kohn-Sham band gap. In Fig. 9 (a) and (b), we show the PDOS for the -1 and -2 charge states for the constrained finite clusters.

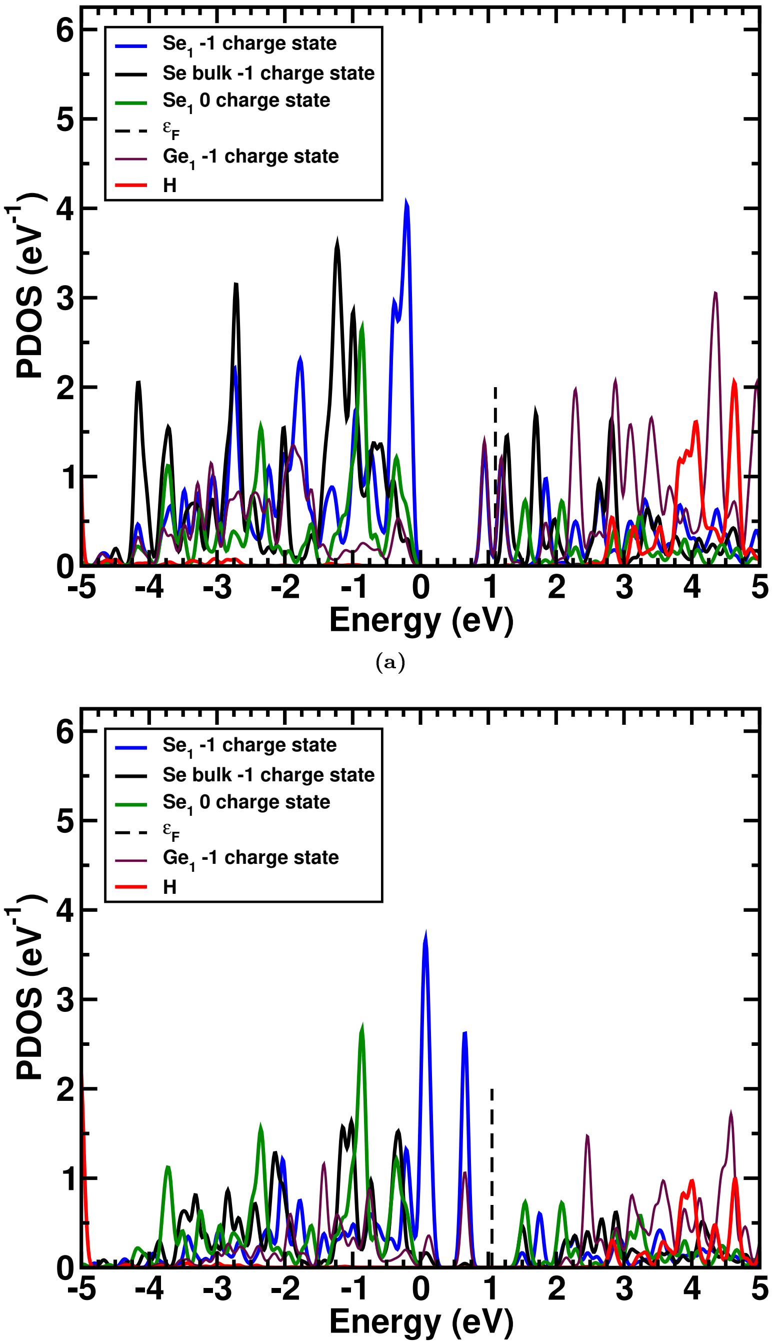

(a)

(b)

Figure 9: PDOS for -1 (a) and -2 (b) charge states for the constrained, PBE cluster calculations

In both figures, the green line is the PDOS on Se$_1$in Fig. 8 in the neutral charge state. This sets the valence band (VB) and conduction band (CB) edges. The VB edge is the zero of energy. In the -1 charge state a gap state appears near the CB edge, while in the -2 charge state, the gap state is in the lower half of the band gap. Note that there is no measurable hydrogen density in the gap states, again demonstrating that the STE is well localized on the interior of the cluster. In Fig. 10, we show the same result in the -2 charge state for the periodic calculation.

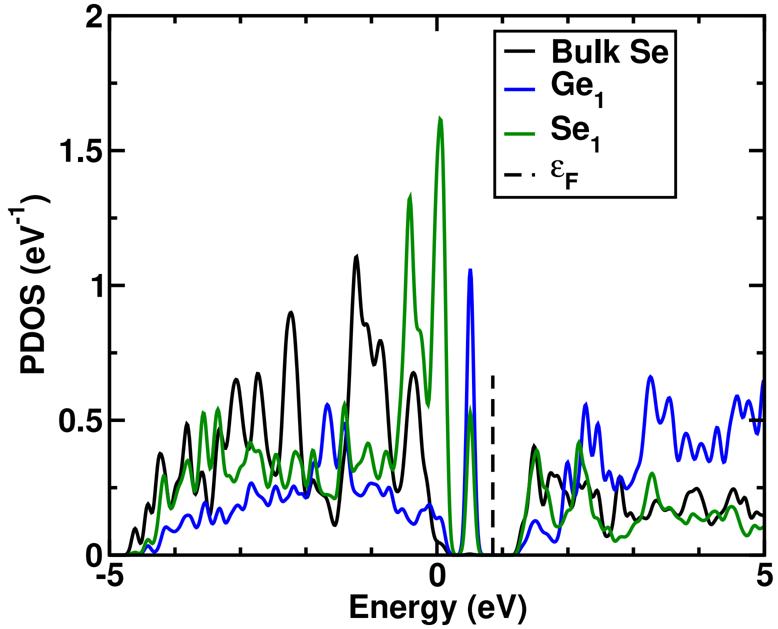

Figure 10: PDOS for the -2 charge state in the periodic calculation

The results are in excellent agreement with those in Fig. 9 (b).

We have calculated the transition state between the stable and metastable equilibria for the unconstrained cluster, and between the two equivalent minima in the constrained cluster. For the unconstrained cluster we used five intermediate configurations in the NEB calculation, while for the constrained cluster we used seven. For the single self-trapped electron, the calculated barriers to motion are 0.17 eV (u) and 0.08 eV (c) in the PBE approximation and 0.33 eV (u) and 0.26 eV (c) in the B3LYP approximation, while for paired STE's, the B3LYP value for the constrained cluster is 0.6 eV. These values are upper bounds on the hopping energies in the small polaron model for two reasons. First, the NEB method always approaches the transition state from above. Second, this is an adiabatic energy that takes no account of electron tunneling. However, even this upper bound precludes self-trapping as a mechanism for completely freezing out electron transport. Using simple kinetic theory, $R = \nu \bullet exp(\frac{-\Delta E}{kT})$, where ν is an attempt-to-escape frequency, ΔE is the calculated barrier, k is the Boltzmann constant, and T is the temperature, we can estimate the hopping rate as a function of T. Alternatively, we can use R^{-1} to estimate a residence time at a single site. We calculated the normal modes, and analyzed those associated with the trapping relaxation. A mode at 77 cm^{-1} (c^{-}) and 172 cm^{-1} ($c^{=}$) exhibited both the appropriate Ge-Se stretch, and the Ge-Ge-Se bond angle distortions localized on the germanium pair of interest. Using the lower B3LYP energy barrier (from the constrained cluster), and the higher attempt-to-escape frequency (from the unconstrained cluster), thus estimating a lower bound on localization, we estimated at 300 K the values in Table 5.

Table 5: Transport parameters from simple kinetic theory in Eq. 4.1.2

	c^-	$c^=$
ΔE (eV)	0.26	0.6
$\nu(\mathrm{cm}^{-1})$	77	172
R (sec^{-1})	$8.8\mathrm{x}10^7$	$4.26\mathrm{x}10^2$
$\tau = \mathrm{R}^{-1}$(sec)	$1.14\mathrm{x}10^{-8}$	$2.3\mathrm{x}10^{-3}$
T (K)	81	186

Using the room temperature hopping rate, and assuming an electric field strong enough to bias every hop in the forward direction, we estimate the transit-time across a 1 μm layer of material of 0.3 sec for single STE's and 4.5 sec for STE pairs. For experiments with time frames on the order of milliseconds, the STE pair would be essentially immobile.

These calculations point to two validation experiments. First, low-temperature electron spin resonance could be used to identify self-trapped electrons. We have calculated the ^{73}Ge and ^{77}Se hyperfine coupling constants for all heavy atoms in the clusters for localized electron conformation. We have also calculated the ^{1}H hyperfine to demonstrate further that the boundary atoms do not participate significantly in electron trapping. The most prominent interactions are shown in Table 6.

Table 6: Calculated hyperfine interactions for atoms labeled in Fig. 7. a_{iso} is the isotropic splitting and b_{1-3} are the principal values of the anisotropic dyadic: $\mathbf{H}_{max}$ is the maximum predicted splitting for the terminating hydrogen atoms: values inside (outside) parentheses are for the constrained (unconstrained) cluster: all values in Gauss

	a_{iso} (G)	b_1	b_2	b_3
Ge_1	156.0 (170.5)	-4.73 (-2.69)	1.48 (0.63)	3.26 (2.06)
Ge_2	31.5 (56.1)	-1.70 (-1.68)	0.78 (0.80)	0.92 (0.86)
Se_1	53.4 (61.7)	-50.0 (-41.67)	-48.8 (-40.55)	98.77 (82.22)
Se_2	25.4 (38.1)	-43.24 (-43.72)	-40.88 (-41.45)	84.12 (85.18)
H_{max}	0.8 (1.25)	0.1 (0.29)	-	-

4.2 Ag in Ge_2Se_3

Because silver is used in several Ge-Se based CBRAM technologies, it is the obvious first metal to study in these systems. We studied both interstitial silver and silver substituting for germanium. We discuss these in turn.

4.2.1 Interstitial Ag

We have studied the simple, interstitial silver (Ag$_I$) in two qualitatively different environments, shown in Figs. 12(a) and (b), which we label Ag$_{I1}$ and Ag$_{I2}$, respectively. In both conformations the interstitial silver bonds only to selenium atoms. The interlayer silver is especially interesting because we argue that there is strong evidence that the silver atom is actually adjacent to a self-trapped electron.

The projected densities of states (PDOS) for Ag$_{I1}$ is shown in Fig. 11. While we include the geometries for both for completeness, they both exhibit similar fundamental properties. In both cases, there is no silver participation in the band gap. Furthermore, the energy level for the highest occupied atomic silver electron is *above* the conduction band edge, so that the 5s electron drops to the top of the conduction band and is then captured by a defect state localized around the two red germanium atoms in Fig. 12 (a) and (b).

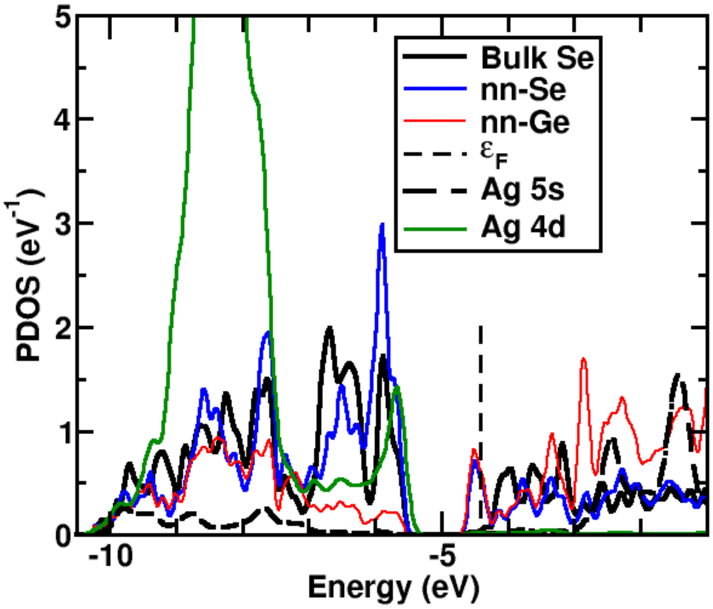

Figure 11: PDOS for the intralayer silver interstitial in the neutral charge state

The Ge-Ge bond length grows by ˜0.1 Å, while the Ge-Se bond lengths grow by $\sim$0.05 Å. The PDOS, shown in Figs. 11 (a) and (b), exhibits one or two peaks very close to the conduction band edge. Both the atomic relaxation and the PDOS spectra are, we argue, fingerprints for electron self-trapping. This autoionization gives a very simple and physical explanation for the persistent mobility of silver in the presence of an electric field, and for its apparent charge state. This behavior is probably quite common in narrow-gap materials, or in highly defective insulators with large numbers of acceptor defect states in the gap.

The positive charge state also explains why silver prefers to bond to negatively charged selenium, rather than to positively charged germanium. Note the similarity between Fig. 11 and Fig. 9 (a). Combined with the changes in the Ge-Ge and Ge-Se bonds indicates that the auto-ionization event leads to the formation of a self-trapped electron. Finally, it is important to clarify that in these calculations, Ag$_I$ is only formally charged *+1*. Mulliken analysis indicates that the predicted net charge is much smaller, about 0.13 e. This is because Ag *5p*-states, which are unoccupied in the isolated atom, admix significantly with the Se *4p*-states near the valence band edge, thus recapturing electron density.

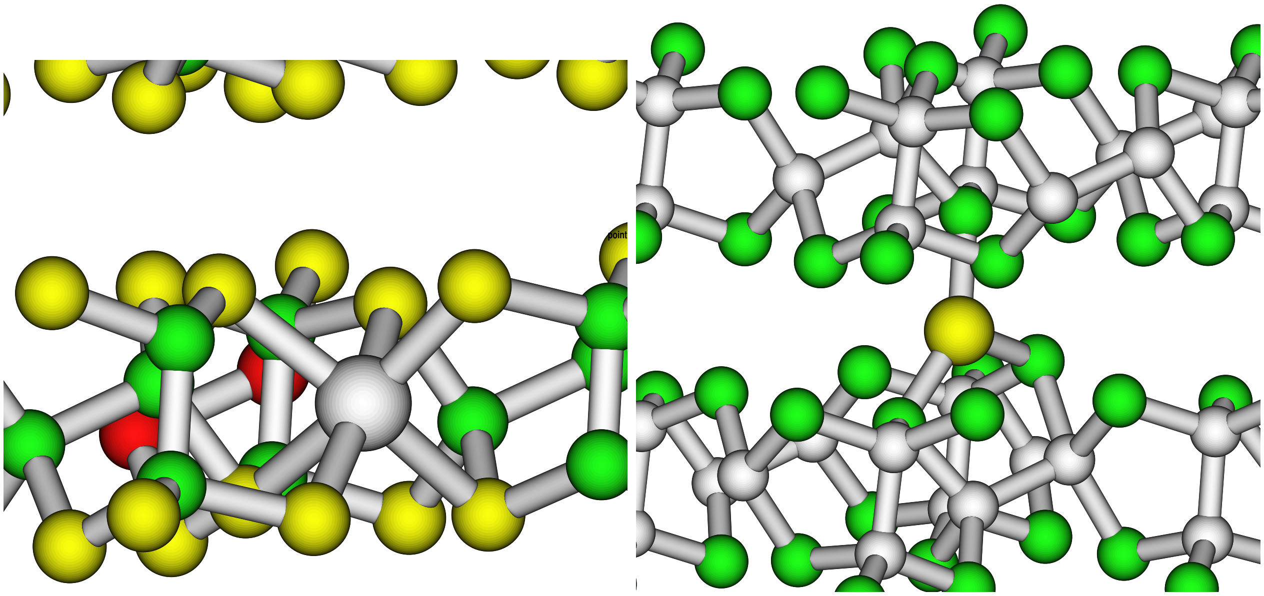

(a) Intralayer

(b) Interlayer

Figure 12: Geometries for the Ag$_I$ in Ge$_2$Se$_3$: extra electron traps on red atoms

To finish this story, we present the equilibrium geometry, in Fig. 13 (a) , and the PDOS, in Fig. 13 (b), for the -1 charge state of the intra-layer silver interstitial.

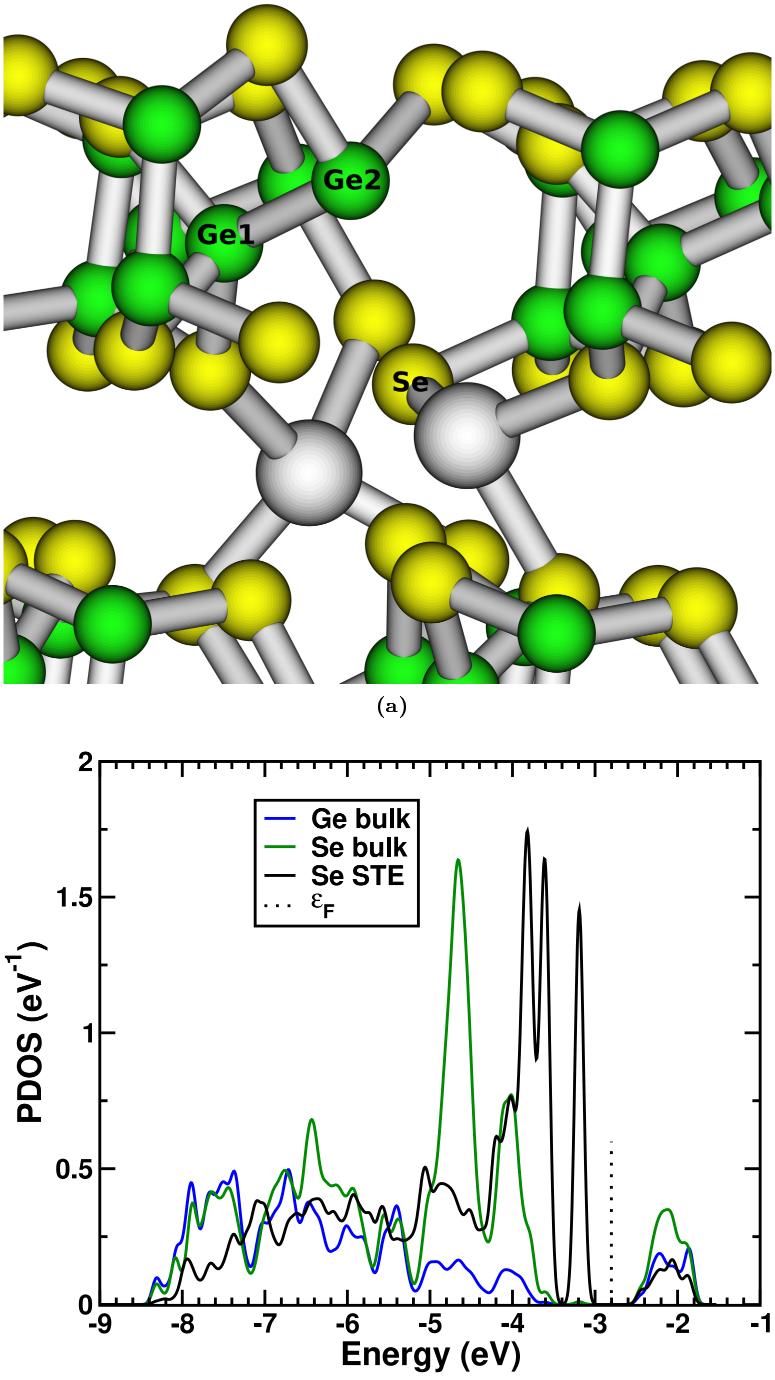

(a)

(b)

Figure 13: Equilibrium configuration (a) and PDOS (b) for -1 charge state of Ag_I in Ge_2Se_3

Comparing the geometry around atoms Ge_1, Ge_2, and Se with that in Fig. 8, and the PDOS in Fig. 13(b) with that in Fig. 10, we argue that best interpretation is that, in the -1 charge state, the silver ion retains a formal +1 charge, and that there is now an STE pair around the Ge_1-Ge_2 dimer.

4.2.2 Substitutional Ag

In Fig. 14, we show. for emphasis, both the initial and the equilibrium configuration of silver substituting for germanium (Ag_S). The defect site undergoes significant rearrangement, including breaking the Ag-Ge bond and forming a new Ge-Se bond, to avoid Ag-Ge bonding. The bond angles ∠Ag-SeI-Ge and ∠Ag-SeII-Ge are reduced to 76° , consistent with considerable strain.

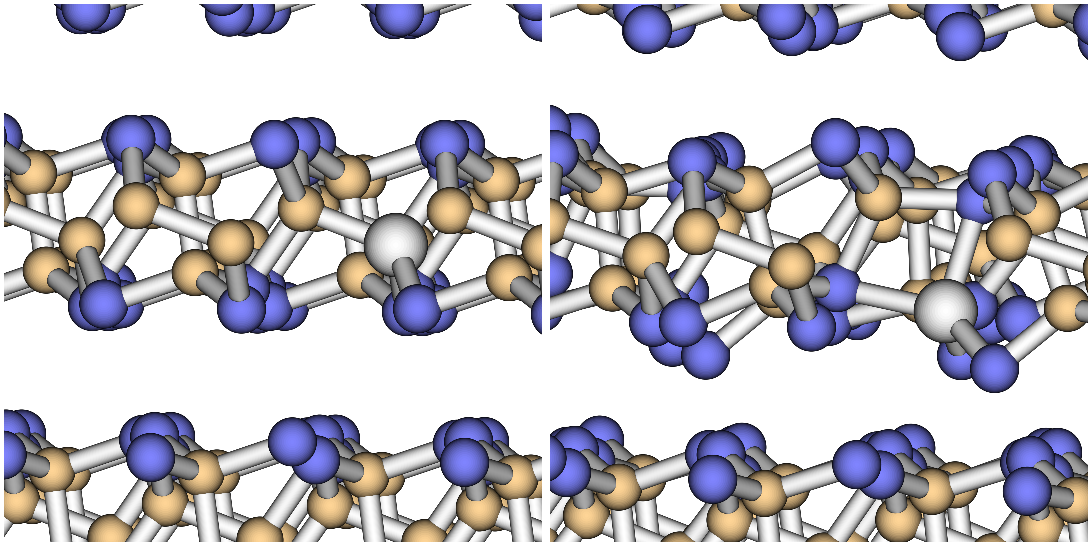
(a) (b)

Figure 14: Ag_S in Ge_2Se_3 in the ideal (a) and relaxed (b) conformations

The electronic structure is shown in Fig. 15. We have included the total PDOS for a bulk selenium atom to delineate the bulk band gap, and to highlight the changes in PDOS for a selenium atom that is adjacent to the silver. We have also decomposed the silver PDOS into *s*, *p*, and *d* components. The Ag-Se bonding creates defect states within 0.3 eV of the Kohn-Sham valence band edge. The bonding is substantially Se *p*-Ag *d*.

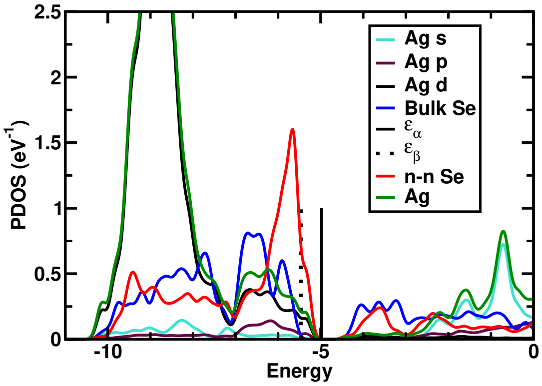

Figure 15: PDOS for Ag_S:Ge in Ge_2Se_3

As a final test case, we considered that possibility of silver knocking a germanium atom into an interstitial site. The initial and equilibrium conformations are shown in Fig. 16. There are three striking features. First, the interstitial germanium forms three bonds with neighboring selenium atoms, although the bond lengths are 0.4 Å longer than normal Ge-Se bonds. This is unsurprising as its nearest-neighbor selenium atoms are three fold-coordinated. Second, there is a substantial bond formed between the silver atom and the germanium atom labeled in Fig. 16(b). In fact, $R_{Ag-Ge}$is 2.54 Å, within 0.05 Åof an analogous Ge-Ge bond.

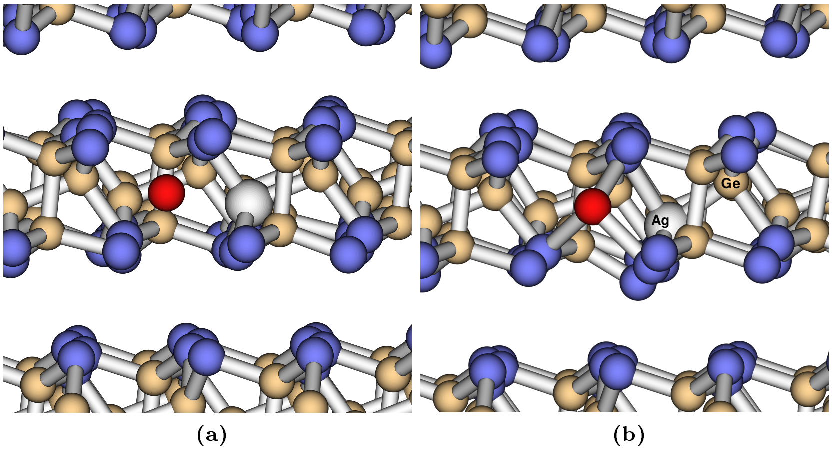

(a) **(b)**

Figure 16: Ag$_S$:Ge$_I$pair in Ge$_2$Se$_3$: (a) undeformed (b)relaxed

In Fig. 17, we show the PDOS for the Ag$_S$:Ge$_I$pair. There are clearly two sets of localized gap states. The lower energy set is derived from the interstitial germanium, its neighboring selenium, and significant silver participation. The second, higher energy, set is derived from silver and its bonded germanium atom, labeled Ge in Fig. 16 (b).

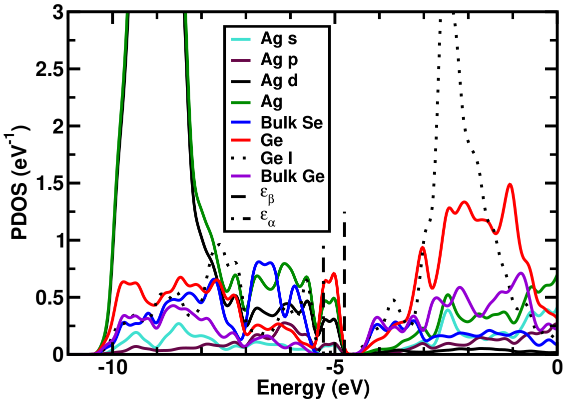

Figure 17: PDOS for Ag$_S$:Ge: Ge is Ge atom bonded to the Ag atom: GeI is interstitial Ge

4.2.3 Formation Energies of Silver Defects

To this point, we haven't discussed the relative stability of these defects. Because they involve gap states, we have to be concerned about stability as a function of Fermi level. To address this, we have used the standard technique of calculating the formation energy, ΔE_f, within the *jellium* approximation, discussed at length elsewhere [28]. The results for silver defects are given in Fig. 18.

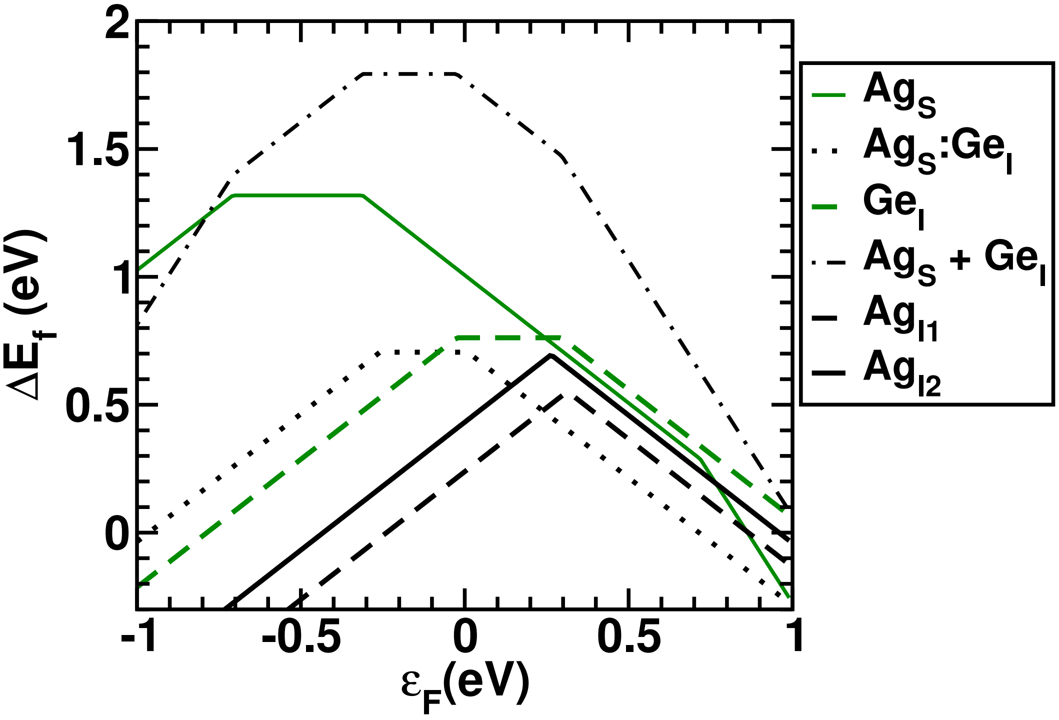

Figure 18: ΔE_f for single Ag atom defects as a function of ϵ_F. ϵ_F=0 for perfect crystal

The slopes of the lines indicate the charge state. Thus, for example, below ~-0.05 eV, the isolated germanium interstitial is positively charged, and between -0.05 eV, and 0.35 eV it is neutral. For all Fermi levels below ~0.2 eV, the lowest energy defect is the intra-layer silver instersitial. However, above that energy the lowest energy defect is the substiutional silver:germanium interstitial. That is, when the Fermi level is roughly 0.2 eV above mid gap, it is energetically favorable for the silver atom to knock a germanium off-site, creating a Ge-Ag pair, and for the germanium atom to become an interatitial. Note that for both the silver insterstitials, there is no Fermi level for which the neutral charge state is stable. This is because of the self-trapping discussed above, and is a direct result of the spontaneous pairing of STE's. This actually complicates our picture of this ostensibly simple defect. Locally, the silver atom is always positively charged, so it might be better only to consider results for the Fermi level within 0.2 eV of mid gap in the upper half of the band gap.

4.2.4 Pairs of Silver atoms

We have studied pairs of silver atoms in the crystalline model of Ge_2Se_3. Here, we have used both 80 and 360 atom unit cells to monitor convergence of geometries and of energies. In all cases here, the 80 atom cell sufficed. This, of course is where we can study the onset of clustering. We considered two distant interstitials, both interlayer (2Ag(inter)) and intralayer (2Ag(intra)), two nearby interstitials (2Ag$_{nn}$(inter) and 2Ag$_{nn}$(intra)), a single interstitial with a neighboring substitutional (Ag$_I$:Ag$_s$:Ge$_I$), and two substitutionals (2Ag$_{s\|}$:2Ge$_I$ and 2Ag$_{s\perp}$:2Ge$_I$, where $\perp$ and $\|$ indicate the Ag dimer is either parallel or normal to the layer surface). As discussed above, in Sec. 4.2.2, the substitutionals we are considering here involve kicking a network germanium into an interstitial position.

Table 7: Energies of formation for pairs of silver atoms in Ge_2Se_3

	$\Delta E_f (eV)$	$\Delta E_f / Ag(eV)$
2Ag(intra)	0.69	0.34
2Ag$_{nn}$(intra)	0.84	0.42
2Ag(inter)	1.02	0.51
2Ag$_{nn}$(inter)	0.99	0.5
Ag$_I$:Ag$_s$:Ge$_I$	0.47	0.24
2Ag$_{s\|}$:2Ge$_i$	0.44	0.22
2Ag$_{s\perp}$:2Ge$_i$	2.25	1.12
Ag(intra)	0.6	0.6
Ag$_s$:Ge$_I$	0.71	0.71

We have included two formation energies for single silver conformations for reference, and we have included a column for formation energy/silver atom. The results indicate clearly that, even for two silver atoms, there is a strong tendency to cluster. The lowest energy is for the formation of a silver-silver dimer with two interstitial germanium atoms. We should note that there is some ambiguity in interpreting these results. In Sec. 4.2.3, we showed that, because there are gap states, we need to consider different charge states, and that formation energies are a function of Fermi level. At the same time, any interstitial silver atom will actually be positively charged, and be accompanied by an STE. In the case of two interstitial silver atoms, there is an STE pair, as implied by the geometry shown in Fig. 19.

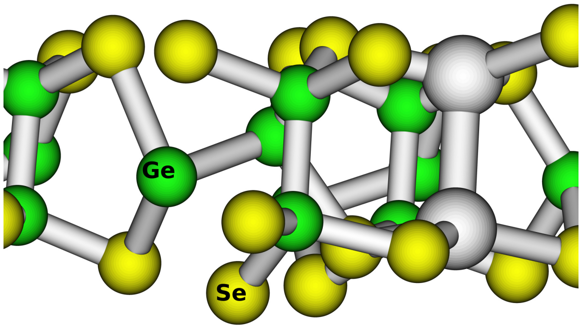

Figure 19: Equilibrium geometry for interstitial Ag dimer

Here, we see the broken Ge-Se bond associated with the STE pair. Never-the-less, the dramatic difference in energy between, say two completely isolated interstitial silver atoms (1.2 eV) and the silver dimer with two interstitial germanium atoms implies that this is the thermodynamically favored conformation.

We conclude this section with a brief discussion of the PDOS for silver pairs. We show in Fig. 20, the PDOS for the configuration in Fig. 19.

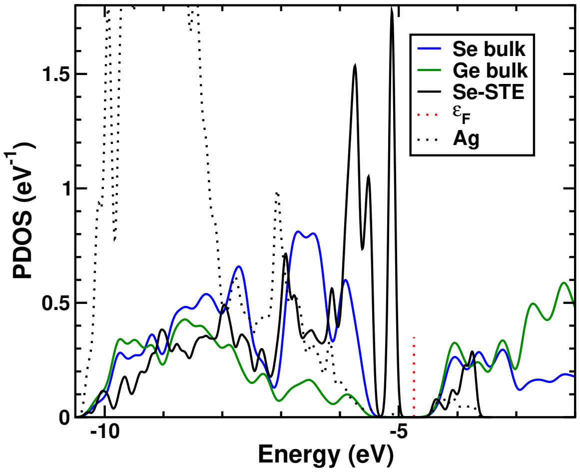

Figure 20: PDOS for interstitial silver dimer as seen in Fig. 19

The blue and green lines set the band edges at approximately -5.5 eV and -4.5 eV. Besides the characteristic peak in the lower half for the STE pair, we note that the PDOS on the silver again shows no appreciable density in the band gap. Moreover, the Fermi level is not pinned by the silver, indicating that the dimer is non-metallic. In Sec. 4.5 below, we discuss the emergence of metallic behavior in silver clusters and dendrites. The current result is simply consistent with our conclusions below.

4.2.5 Sn in Ge_2Se_3, and its Interaction with Ag

Campbell has hypothesized that in Ge_2Se_3, silver attacks the Ge-Ge dimers, and that these sites are the initial seeds for metallic silver growth. This is supported by the results in 4.2.4. However, Campbell has also found that the presence of tin in the material also aids in the stable formation of conductive dendrites. We have explored how tin can be incorporated into Ge_2Se_3 as both substitutionals and interstitials, and how this might interact with silver. In Figs. 21 (a) and (b), we show the equilibrium geometry and the PDOS for the tin interstitial.

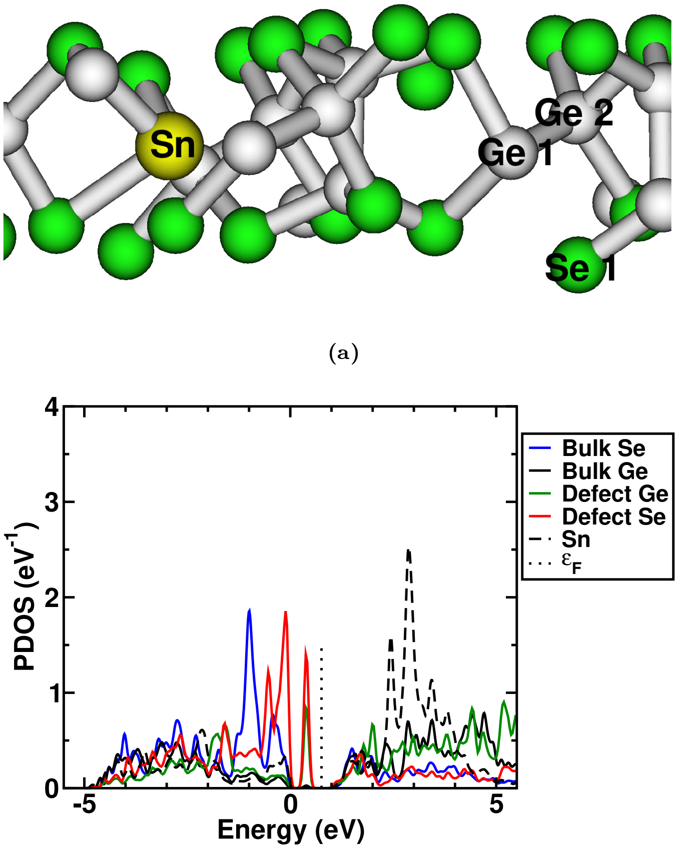

(a)

(b)

Figure 21: Geometry (a), and PDOS (b) for interstitial Sn in Ge_2Se_3

The combined geometry and PDOS indicate that interstitial tin auto-ionizes, dropping two electrons into the conduction band, and that these subsequently become an STE pair. There is negligible tin density in the band gap, similar to silver. In Fig. 22, we show the formation energies of several defects containing tin, and containing tin and silver.

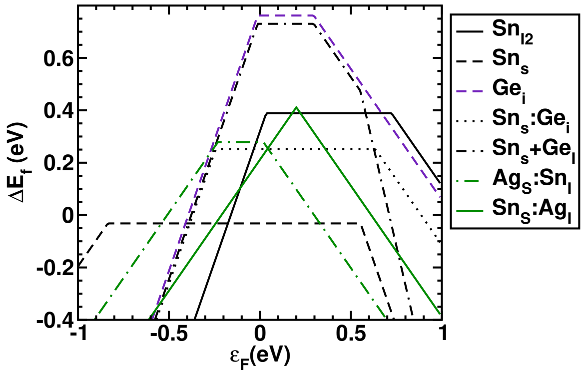

Figure 22: Energies of formation for tin-containing defects in Ge_2Se_3

Several features bear comment. First, the interstitial tin is *exothermic*, so that if metallic tin were deposited on top of Ge_2Se_3, it would be spontaneously absorbed giving of significant einergy of reaction. The absence of the -1 charge state as seen by the kink in the ΔE_f curve at ˜0.6 eV is, again evidence of the instability of a single STE relative to STE pairs. Another striking feature is that formation energy of a silver substitutional is lowered significantly in the presence of an intersitial tin. Furthermore, the formation energy of a silver interstitial is lowered in the presence of a substitutional tin atom. Left to calculate is the energy of a tin-silver dimer. However, these results are consistent with tin facilitating silver incorporation.

4.3 O interactions:Thermodynamics

We first consider isolated substitution of oxygen for selenium. We would expect this to be favorable because oxygen and selenium are isoelectronic. We have calculated energies of formation for all twelve symmetry-unique selenium atoms. The principal results are given in Table 8.

Table 8: Theoretical geometries and energies of formation for oxygen substitutional and bond-centered interstitial. Standard deviation in parentheses

	O_{Se}	O_{Se}:Se_i	$O_{i-Se-Ge}$	O_{Se-O}	$O_{b-c\perp}$	$O_{b-c\parallel}$
ΔE_f (eV)	-1.62 (0.06)	-1.36	0.112	-0.864	-1.73	-2.20
<R_{O-Ge} >(Å)	1.814	1.813	1.986	1.790	1.773	1.764
$< Ge - O - Ge$(deg.)	123.6	110.2			102.1	133.8
R_{O-Se}(Å)			1.83	1.977		

While we give the total average and standard deviations for energies for formation, ΔE_f, and for geometries, there is a trimodal distribution. That is, there are really three energetically different sites, which we label, from low to high, as (a)-(c). Note that the variation in energy of formation follows monotonically the variation in average bond length for the two Ge-O bonds comprising the bridge. Thus, we have the unsurprising result that binding energy follows average local strain. However, this range is important when considering whether substitutional oxygen atoms cluster.

We have considered another oxygen substitutional motif, where the oxygen actually knocks a selenium atom out of its network site to create an oxygen substitutional- selenium interstitial pair (O_{Se}:Se_I). We have considered only one of the three possible oxygen substitutional sites (O_{Se}(c)). As seen in Table 8, the reaction is still strongly exothermic. The final geometry is shown in Fig. 23 .

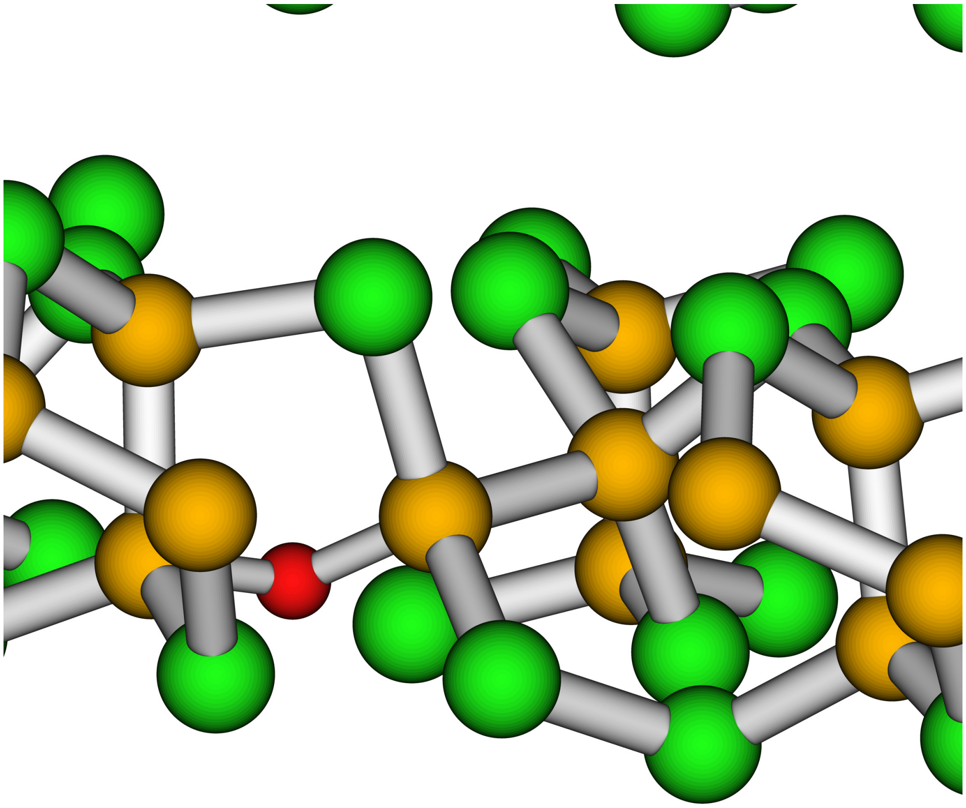

Figure 23: Geometry of O_{Se}:Se_I O is red, Se is green, and Ge is gold

Note that the initially interstitial selenium atom has been incorporated into the network as a Ge-Se-Se-Ge chain. This flexibility probably accounts for the exothermicity.

Interstitial oxygen, O_I, is highly reactive. Depending on the details of the initial geometry, we found a variety of final configurations, simply reflecting which selenium atom facing the interstice was nearest. In Fig. 24, we show the final geometry for one interstitial calculation.

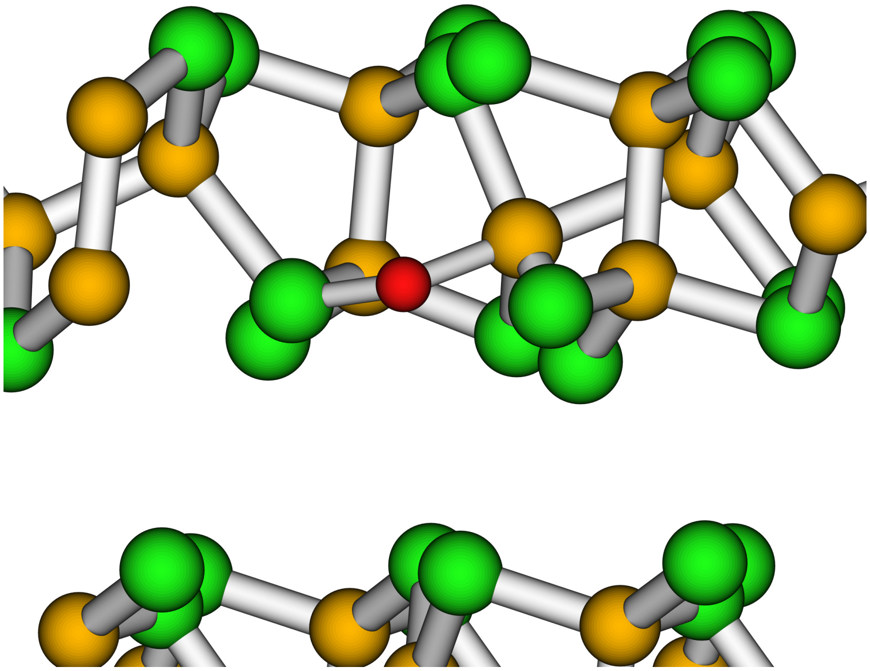

Figure 24: Geometries for one $\mathbf{O}_I$ conformation, $\mathbf{O}_{i-Se-Ge}$

In Fig. 24, the oxygen has bonded to a selenium atom, giving rise to a three fold coordination, with concomitant weakening of the two Ge-Se bonds, along with significant bonding to a germanium atom. In fact, the Ge atom is in the expected geometry for five fold coordination- three Se ligands in a planar geometry and two ligands, the oxygen atom and one selenium atom, in pyramidal positions. Other more stable equilibria are found if we force the oxygen to be near near either $D_\perp$ or $D_\|$. In that case, the oxygen spontaneously forms a Ge-O-Ge bridging moiety within the dimer. Because of the possibility of multiple local equilibria, we used four initial geometries. In each case, the oxygen atom was centered between the two Ge atoms comprising the dimer, 1.05 Å from the bond center, but rotated $\frac{\pi}{2}$ radians around the dimer axis. We did this for both the $D_\|$and $D_\perp$ conformations. Independent of the initial geometry there was only one equilibrium geometry for $D_\perp$. This is not surprising, if we note that the six selenium atoms surrounding $D_\perp$ should determine the direction of the Ge *sp*-hybrid normal to the plane of the three nearest neighbor selenium atoms. Note that spontaneously the oxygen atom takes a bond-centered configuration, denoted by either $O_{b-c\|}$ or $O_{b-c\perp}$. The energy of formation for $O_{b-c\|}$ is -2.20 eV, significantly more exothermic than any of the substitutional conformations. Also, note that the two conformations $O_{b-c\|}$ and $O_{b-c\perp}$ have significantly different structures and stabilities. This is explained easily by noting that $D_\perp$ is significantly more stable initially, with $R_{Ge-Ge\perp} < R_{Ge-Ge\|}$, so that the bridge is more highly constrained geometrically. In an amorphous structure we can expect at least this range in stability and structure. Never-the-less, based on these results, we would expect that, thermodynamically, oxygen atoms would fill all Ge-Ge dimers before forming any other species. Finally, we find that when oxygen is placed near enough to a Ge-Se pair, it will form a Ge-Se-O-Ge structure with an energy of formation of -0.87 eV (exothermic).

4.3.1 O interactions: Kinetics

Our most recent work deals with the kinetics of oxygen in this crystalline model of Ge_2Se_3. The work discussed in Sec. 4.3 appears to predict that oxygen atoms will first be trapped by selenium atoms, and then, if the barriers are small enough, to migrate to the Ge-Ge dimers and to form Ge-O-Ge bridges. Furthermore, after all dimers are transformed to Ge-O-Ge bridges, oxygen atoms can then displace selenium atoms *exothermically* to become part of the existing network. However, if the kinetic barriers are too high, oxygen will remain in interstitial conformations similar to that in Fig. 24. To complete this picture, we clearly need to calculate barriers to reactions. While this work is still in progress, we can report on a few reaction paths leading to incorporation of interstitial oxygen into the network. In Fig. 25 , we show the approximate reaction path predicted by the NEB method, and, in Fig. 26, the crucial geometries of the path. Note at the top of the path (2), one Ge-Ge bond and one Ge-Se bond break before the oxygen atom bridges the two atoms.

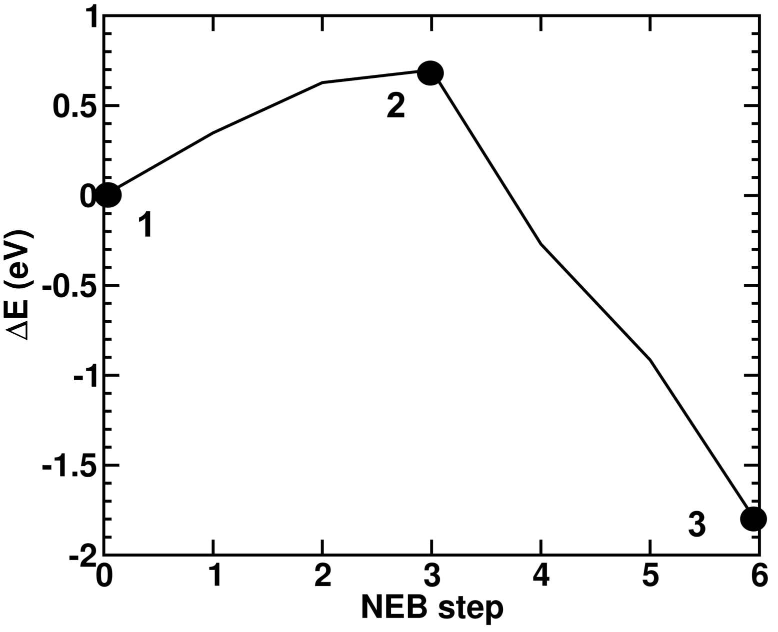

(a)

Figure 25: Potential surface for O incorporation: geometries for (1), (2), and (3) in Fig. 26 (a)-(c)

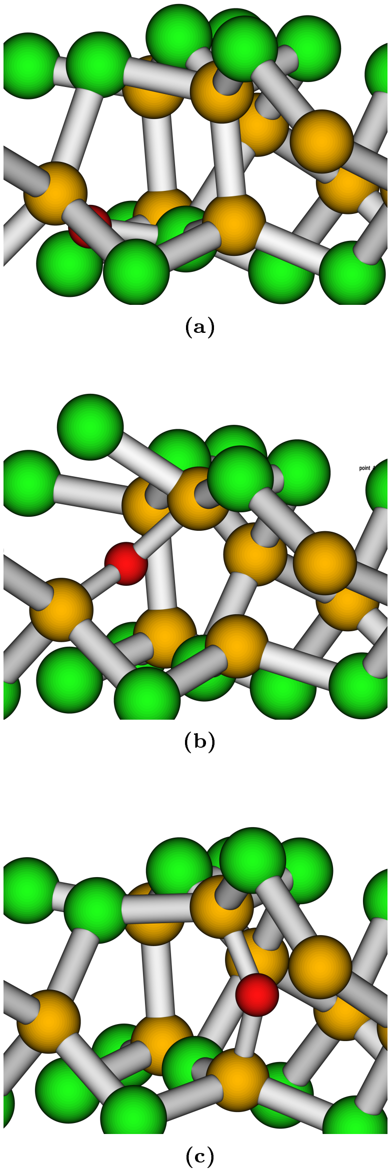

Figure 26: Geometries associated with initial (1), peak (2), and final(3) energies in Fig. 25

The estimated kinetic barrier, 0.7 eV, is low enough that this reaction should take place readily at room temperature. We should point out that with a small perturbation of this reaction path, there is another metastable state into which the oxygen can fall, shown in Fig. 27, where it forms a Ge-O-Se-Ge bridge. From this geometry, the oxygen can move, over a barrier of 0.7 eV, to a bridging position on the neighboring $D_{\|}$. This is We have calculated a reaction barrier from directly from the geometry in Fig. 27 to the bridging position shown in Fig. 25 (d). The activation energy for this path is ~1.65 eV– so high that this path would not be accessible at RT.

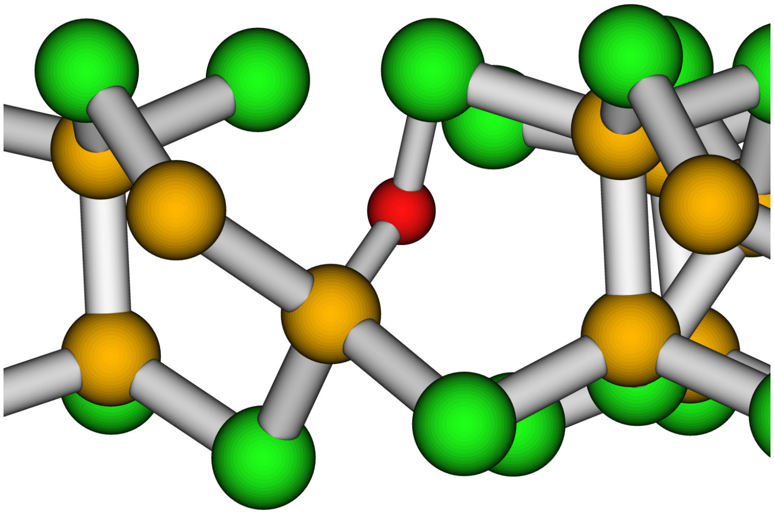

Figure 27: Metastable configuration accessible at RT from the interstitial state in Fig. 24

However, that the barrier for a nearest-neighbor hop is relatively modest, ~0.6 eV, suggests that we look for a path that involves several single site hops. We have also calculated a reaction path from the interstitial site to the substitutional geometry shown in Fig. 23. Again, this direct reaction path devolved into two separate reactions. The first was to another Ge-O-Se-Ge bridging position. From here, the oxygen simply pushes the neighboring selenium atom into the Ge-Se-Se-Ge configuration. That knock-on reaction barrier was ~1.63 eV from the equilibrium geometry , and reflects that the Ge-O-Se-Ge conformation is much more stable than the interstitial conformation. So, while O$_S$-Se$_i$ is thermodynamically more stable, it may not be observed. This is reinforced by the possiblity that there are two accessible, single-site jumps to another Ge-O-Ge conformation. Clearly, we need to complete our investigation into hops between neighboring Ge-O-Se-Ge sites. If these are similar to the hop from Ge-O-Se-Ge (Fig. 27) to Ge-O-Ge$_{\|}$, then the model of oxygen motion is fairly simple. The initial interstitial configuration (Fig. 24) would be very short-lived. The modest barriers mean that the oxygen would find one of several sites, and could be relatively mobile until it makes a hop into a Ge-O-Ge bridge. Given the deep potential wells, it appears unlikely that a Ge-O-Ge$_{\perp}$ would readily transform into a Ge-O-Ge$_{\perp}$. Translating this to an amorphous solid, we would predict that any Ge-Ge dimer would be an oxygen trap that would demobilize an oxygen atom at or near RT. Put slightly differently, oxygen will remain mobile until it encounters a germanium dimer. This means that, not only thermodynamically, but kinetically, oxygen will find and fill all germanium dimers.

4.3.2 O_2 interactions: Thermodynamics

While interaction with a single oxygen atom is potentially simpler than the interaction with an O_2 molecule, the interaction with O_2 is technologically more interesting because we would expect oxygen to enter as O_2, either from an exposed surface, or through diffusion from, say, surrounding SiO_2. The first question of interest is whether O_2 diffuses readily through the system. We should note that O_2 diffuses as if it were inert in a-SiO_2[23, 29, 9]. It's diffusion coefficient is quite close to that of Kr, which is roughly the same size as molecular oxygen (see Ref. 36 in [9]). We have considered a variety of initial geometries, including interlayer O_2 and intralayer interstitial sites. We should note that the ground state of the oxygen molecule is a spin triplet. We have performed some calculations in the triplet state, and other than for isolated $O_{2,}$, there was no case where the triplet was lower in energy than the singlet. We assume that there is an intersystem crossing upon entering Ge_2Se_3.

In Fig. 28, we show the initial and final geometries for an interlayer oxygen molecule.

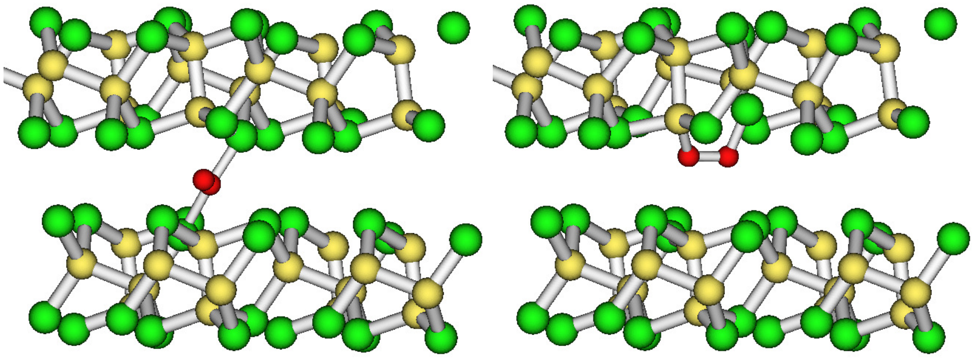

(a) (b)

Figure 28: Initial (a) and final (b) geometries for an interlayer oxygen molecule

The molecule stays intact, but joins the network as a peroxyl linkage between a selenium atom and a germanium atom. For an intralayer O_2, shown in Fig. 29, the peroxyl linkage is between two germanium atoms.

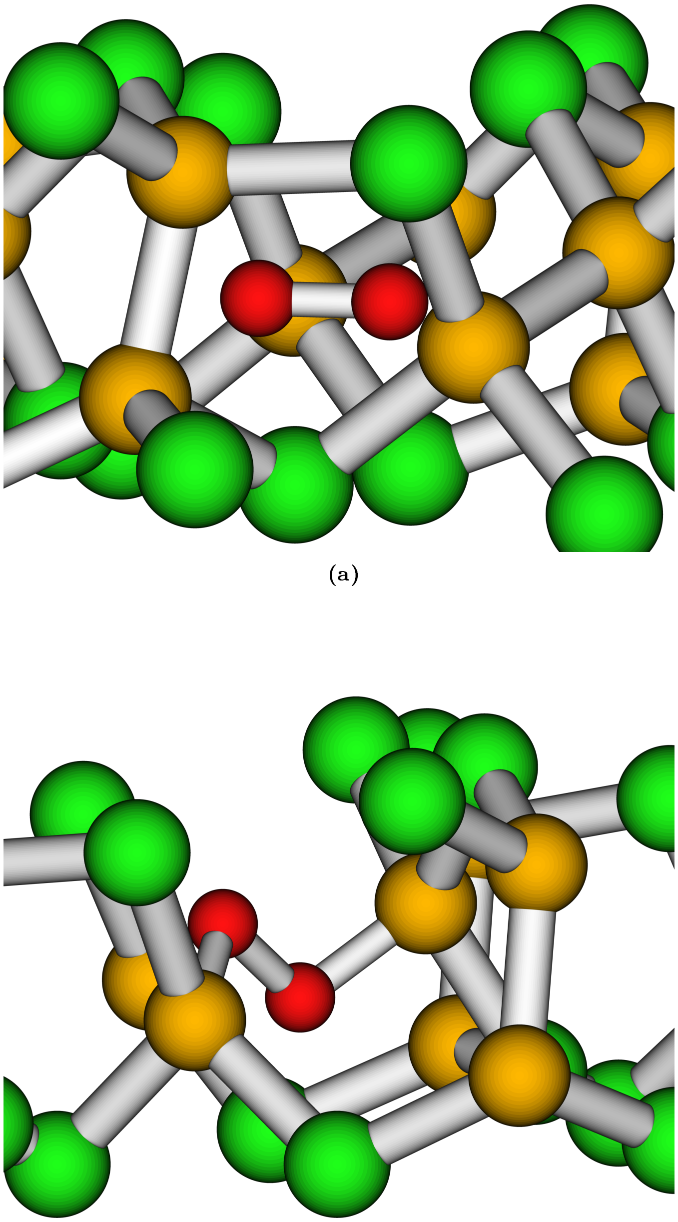
(a)

(b)

Figure 29: Initial (a) and final (b) geometries for the intralyer O_2 interstitial

In Table 9, we show the geometries and energies of formation, per oxygen atom, for various O_2 conformations.

Table 9: Geometries and energies of formation for O_2 interstitial

	O_2interlayer	O_2intralayer (singlet)	O_2intralayer (triplet)	O_2intralayer interstitial
ΔE_f (eV)	-0.078	-0.265	0.452	0.33
R_{O-O} (Å)		1.51	1.51	1.3
R_{O-Ge} (Å)		1.81		

With the exception of O_i shown in Fig. 24, the peroxyl conformations are much less energetically favored than any of the single oxygen conformations. To finish this work, we need to calculate the kinetic barriers from a peroxyl linkage to separated oxygen defects. The obvious first step is to study how the peroxyl linkage becomes a single bridging oxygen and a neighboring Ge-O-Se-Ge moiety.

4.4 Cu and Ag in SiO_2

Because $SiO_2$and copper are already part of standard silicon processing, there is significant motivation to use these materials to replace chalcogenide-based elelctrolyte-silver materials at the core of CBRAM devices. We have studied both silver and copper in α-quartz and in an amorphous model of SiO_2, although we have studied copper more fully because of its current use in memristive devices. For copper, we have identified local intersitital equilibria for several charge states, and we have calculated barriers to motion in both the +1 and +2 charge states. We have used the open c-axis channel as a first approximation for porous a-SiO_2.

4.4.1 Interstitial geometries

In Fig. 30, we show the equilibrium configuration for neutral copper in an interstitial space in α-quartz. In Table 10, we show the pertinent relevant parameters as a function of charge state, using the labels in Fig. 30.

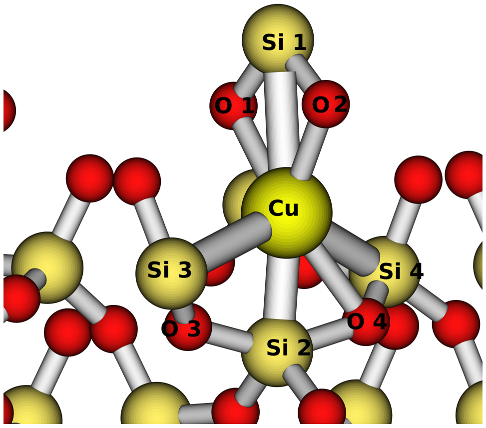

Figure 30: Equilibrium geometry of neutral copper interstitial in α-quartz

Only in the neutral state was there significant interaction between the copper atom and the host lattice, where Si_2 bonded with copper and the O_3 and O_4 moved out to accomodate the bond. In both the $+1$ and the $+2$ charge states, the O-Si-O bond angles and the Si-O bond lengths rearranged close to the crystalline values. In all cases there was expansion of the c-channel around the copper atom/ion, as seen by the increased Si-Si bond lengths in Table 10 We sampled several other initial geometries and obtained results within ~0.1 meV across charge states. All of these are along the c-axis channel.

Table 10: Geometric parameters as a function of charge state for interstitial copper in $\alpha-$quartz: numbering as in Fig. 30

	$\alpha - quartz$	Cu^o	Cu^{+1}	Cu^{+2}
$R_{Si_1-Si_2}$	5.00	5.14	5.31	5.32
$R_{Si_3-Si_4}$	5.48	5.70	5.54	
R_{Cu-Si_2}	-	2.29	2.81	2.83
$R_{O_1-Si_1}$	1.64	1.66		
$R_{O_3-Si_2}$	1.65	1.75	1.65	
$\angle O_1 - Si_1 - O_2$	108.0	99.8	103.7	98.0
$\angle O_3 - Si_2 - O_4$	109.24	150.9	105.3	95.0

4.4.2 Barriers to motion

In Figs. 31 (a) and (b) ,we show the energy landscape between two neighboring equilibrium positions.

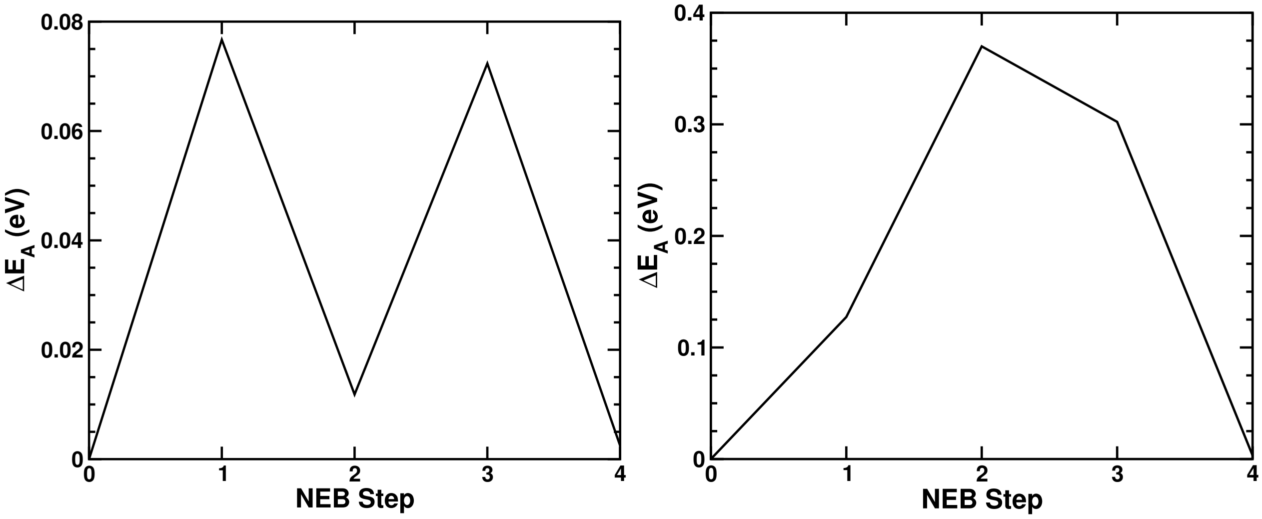

(a)

(b)

Figure 31: Reaction path for Cu^{1+}(a) and Cu^{2+} (b)

The activation energies for motion for Cu^{1+} and Cu^{2+} are 0.078 eV and 0.37 eV respectively. Clearly Cu^{+1}will be damatically more mobile.

4.5 Study of Dendritic Conductivity

As noted in Sec.4.2.4 , diatomic silver is non-metallic. It turns out that small clusters of silver are also non-metallic. In fact, previously, it was shown that the HOMO-LUMO gap narrows to thermal energies only for clusters larger than forty atoms. Because the standard cartoon model envisions a monomeric filament becoming conductive, we started by asking how long a filamentary cluster is required for metallic behavior. We performed quantum calculations on finite clusters of atoms, starting with linear monomers. Using GAMESS [35], performed standard Hartree-Fock, density functional calculations, using the B3LYP exchange correlation potential, and configuration interaction using all singly excited Slater determinants (CI-singles). In Fig. 32, we show the first excitation energy as a function of cluster size for linear and for helical clusters. In all cases, the cluster geometries were allowed to relax to seek a minimum energy configuration. Two features bear mention. First, for the linear cluster, the first excitation energy appears to approach approximately 1.0 eV assymptotically, for large cluster sizes. In retrospect, this is expected, if we think about the tight-binding picture. The interactions between any atom, and more distant neighbors will die off rapidly. For a more complex geometry, we find a surprising scatter. However, even at 10 atoms, the first excitation gap becomes vanishingly small.

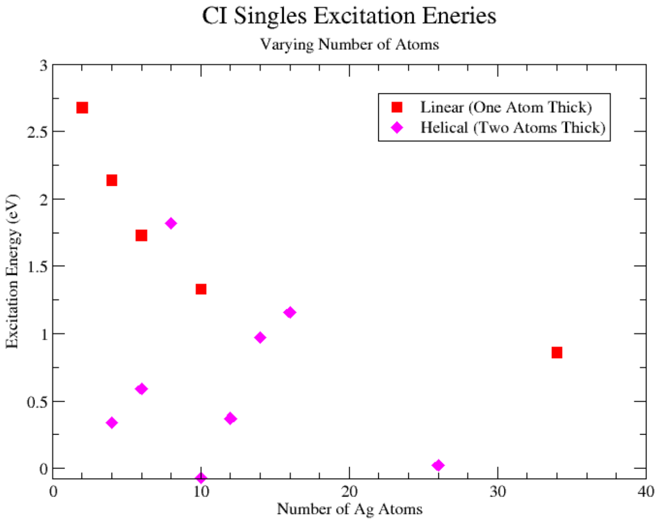

Figure 32: CI-singles results for linear and helical clusters, as a function of cluster size

We also performed some periodic calculations. Here, all systems were perfectly linear. The variation was dendrite thickness. We used SEQQUEST, the PBE exchange correlation potential [30], and a double-zeta quality basis set with polarization functions. We performed spin polarized calculations. In Fig. 33, we show the spin-projected PDOS on a single silver atom.

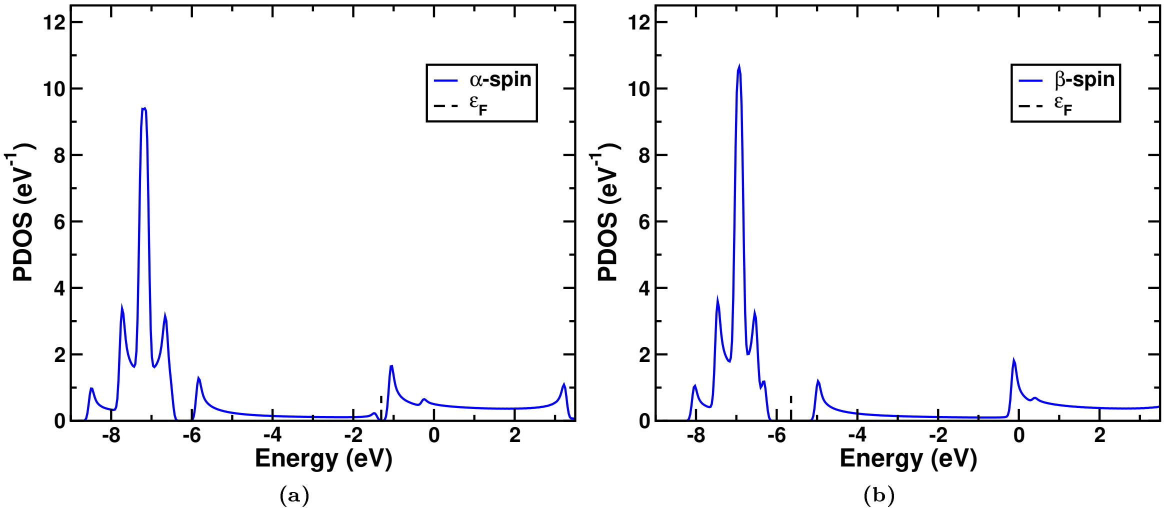

(a)

(b)

Figure 33: Spin projected PDOS for infinite linear monomer: (a) α-spin (b) β-spin

Absent magnetic mixing, this periodic case agrees qualitatively with the finite cluster results. Thus, at least for an isolated monomer, we expect no metallic conduction. We have already shown above that, even for small clusters (~tens of atoms), we can expect to see metallic behavior. In Fig. 34, we show a linear dendrite with a three-atom primitive cell, and the calculated PDOS.

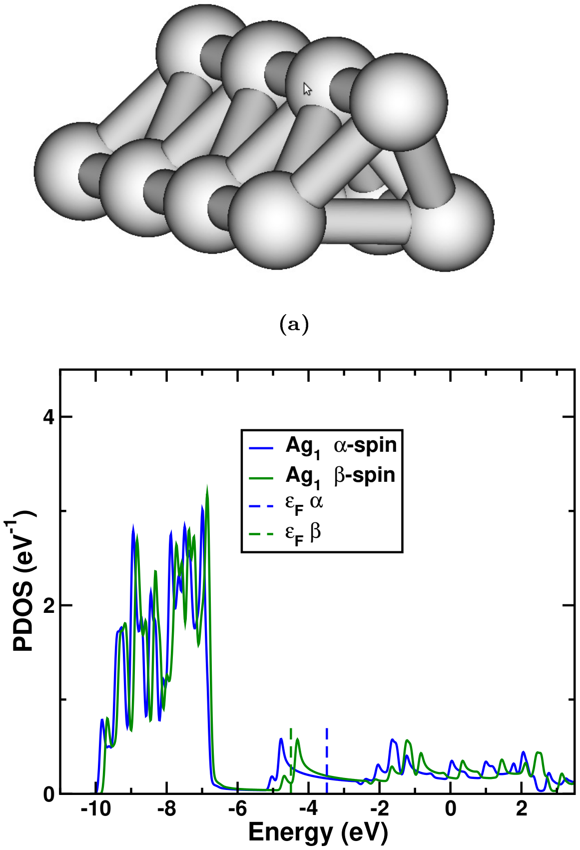

(a)

(b)

Figure 34: Cross-section (a) and PDOS (b) for dendrite with three-atom primitive cell

Clearly, even a three atom thick dendrite, we are seeing metallic behavior for infinite dendrites. Two points merit amplification. First, our results on unimbedded silver clusters and dendrites indicate that isolated atomic, or even diatomic, silver in the solid will not be metallic. The distortion of the local electric field will probably be small. Second, relatively small clusters of silver atoms do become metallic. In future work, we should calculate actual conductivities of dendrites as a function of thickness. We should calculate the AC conductivity of the finite clusters for which we predict zero band gap. Finally, we should consider the effects of embedding, although the results in Fig. 20 are consistent with these bare dendrite results.

4.6 Device Modeling: Compact Model for CBRAM

We pursued developing a compact model for the simple device shown in Fig. 1, building on Yu and Wong's original work [42]. The operating mechanism of the PMC model is visualized in Fig 35.

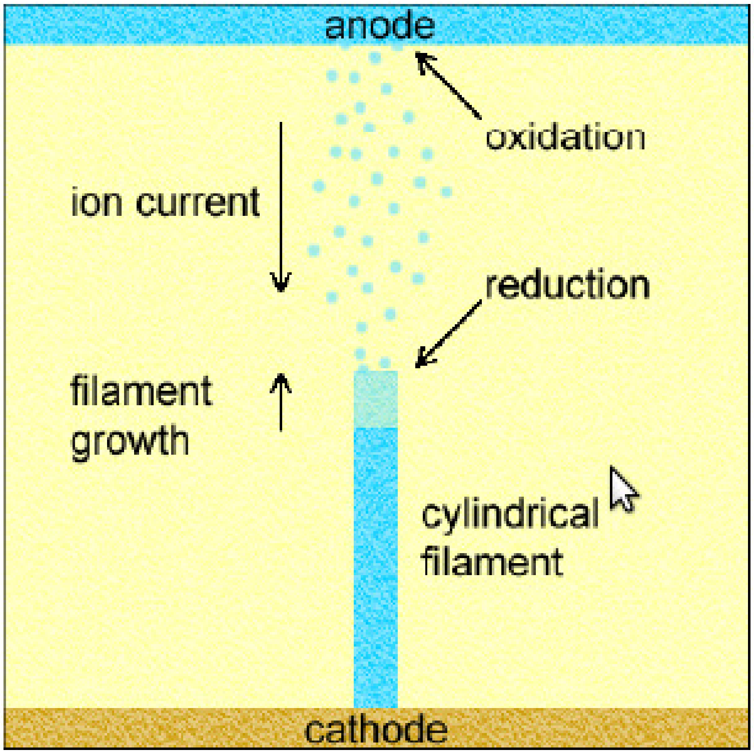

Figure 35: Operating mechanism of PMC model

The model uses a time-stepping procedure with analytical equations for resistance that evolve over time to obtain the model's behavior. The Mott and Gurney ionic hopping current [26] is assumed to be the rate limiting process in the PMC. Therefore, the Butler-Volmer charge transfer equation [10] is not incorporated, but it could be if necessary. All of the ionic flux is assumed to reduce on the filament, which is modeled as a cylinder with adjustable height and radius. The filament height is adjusted each time step in proportion to the ions accumulated during the step and the concentration of neutralized ions in the filament. The radius can change once the filament has connected the anode and cathode.

4.7 Structure and Resistance Model

The resistance model calculates the total resistance of the PMC given the dimensions and material properties of the cell and filament. The simulation structure is modeled after an ASU PMC that is a cylindrical cell with a diameter of 5 µm and a ChG electrolyte thickness of 60 nm. The height and radius of the filament are variables during the simulation. As can be seen in the I-V data in Figs. 10-11, the PMC has a diode characteristic in the OFF and ON states. The electrolyte and filament are modeled as separate diodes in parallel. The resistances of the diodes are calculated using the Shockley ideal diode equation with quality factor and added series resistance. The electrolyte series resistance is given by

$$R_{se} = \rho_e \cdot L/(\pi \cdot (r_{cell}^2 - r^2)), \tag{1}$$

where ρ_e is the resistivity of the electrolyte, L is the electrolyte thickness, r_{cell} is the radius of the PMC, and r is the radius of the filament. The series resistance of the filament (Eq. 1) is calculated as two resistors in series – the resistance of the neutralized ion portion of the filament and the resistance of the electrolyte in the cylindrical space remaining between the filament and the anode.

$$R_{sf} = (\rho_f \cdot h + \rho_e \cdot (L - h)/(\pi \cdot r^2), \tag{2}$$

where ρ_f is the resistivity of the filament and h is the height of the filament. The resistances of the electrolyte and filament diodes are given by (16) and (17), respectively, where V is the applied anode voltage. An insignificant value, *10*$^{-16}$, is added to the diode current to avoid a division by zero error.

$$R_f = V \cdot \left[I_{sf} \cdot \left(\exp\left(\frac{V}{n_f kT} \right) - 1 \right) + 10^{-16} \right]^{-1} + R_{sf} \tag{3}$$

$$R_e = V \cdot \left[I_{se} \cdot \left(\exp\left(\frac{V}{n_e kT} \right) - 1 \right) + 10^{-16} \right]^{-1} + R_{se} \tag{4}$$

The total resistance of the PMC (Eq. 5) is the parallel combination of Eqs. 3 and 4.

$$R = (R_f^{-1} + R_e^{-1})^{-1} \tag{5}$$

Table 11 summarizes the parameter values used in these equations. The filament material is assumed to be Ag_2Se for which the resistivity was extracted from Ref. [18]. The other values besides the dimensions where chosen to approximately fit Eq. 5 with the data in Figs. 36 (a) and (b).

Table 11: Parameters for structure and resistance

Parameter	Value	Unit	Description
ρ_f	$7x10^{-4}$	$\Omega - cm$	Filament resistivity
ρ_e	$8x10^{-4}$	$\Omega - cm$	Electrolyte resistivity
L	$6x10^{-6}$	cm	Electrolyte thickness
r_{cell}	$2.5x10^{-4}$	cm	Cell radius
I_{sf}	$1.8x10^{-6}$	A	Reverse saturation current
I_{se}	$1.8x10^{-9}$	A	Reverse saturation current
n_f	1	-	Diode quality factor
n_e	1	-	Diode quality factor

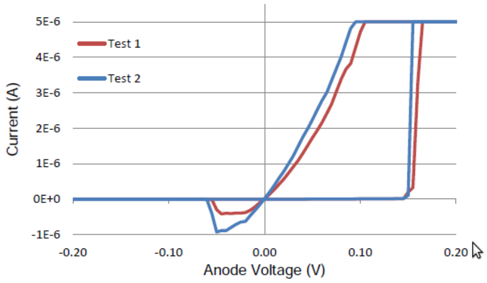

(a)

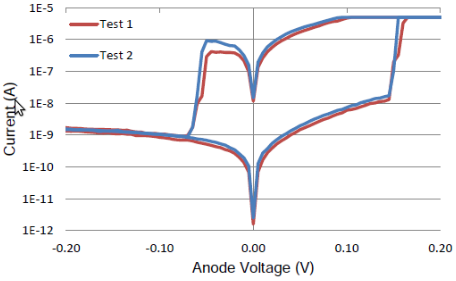

(b)

Figure 36: Experimental I-V characteristics of two consecutive write-erase cycles of a typical PMC: (a) linear-linear (b)log-linear

4.8 Filament Growth

The filament grows and dissolves according to the flux of Ag$^+$ (j_{hop}) given by Eq. 6

$$j_{hop} = 2zeca\omega \left(-\frac{W_a}{kT}\right) \sinh\left(\frac{E \cdot ez \cdot a}{2kT}\right), \tag{6}$$

where c is the concentration of mobile ions with charge ze, a is the hoping distance, ω is the attempt-to-escape frequency, W_a is the activation energy, E is the electric field, and kT is the thermal energy, and to the concentration of Ag in the filament. However, polarity dependent activation energy is used in to account for the asymmetric OFF/ON switching voltages seen in Fig. 36 (a). An asymmetric energy barrier is suggested in Ref. [15] as a possible cause for this behavior. The electric field used in Eq. 6 is given by Eq 7.

$$E = V/(L + h \cdot (\rho_f/\rho_e - 1)). \tag{7}$$

The temperature of the cell, used in (3), (16) and (17), is given in Eq. 8

$$T = T_o + V^2 R_{th}/R, \tag{8}$$

where T_0 is the equilibrium temperature, V is the applied anode voltage, R_{th} is the equivalent thermal resistance, and R is the total cell resistance. The concentration of Ag in the Ag_2Se filament is given by

$$N_{Ag} = 2N_A \cdot \rho_{Ag2Se}/m_{Ag2Se}, \tag{9}$$

where N_A is the Avogadro constant, and ρ_{Ag2Se} and m_{Ag2Se} are the density and molar mass of Ag_2Se, respectively. When the PMC is non-bridged, the growth velocity of the cylindrical filament height is given by

$$\nu_h = j_{hop}/(zqN_{Ag}) \tag{10}$$

When the PMC is bridged, the electric field in Eq. 6 is replaced by the applied anode voltage multiplied by a fitting parameter, because there is no longer a gap between the electrodes with which to calculate electric field. An electric field must still exist in order to grow and dissolve the filament radius. Similar to Eq. 6, the ionic hopping current density for the on-state is

$$j_{hop-on} = 2zeca\omega \left(-\frac{W_a}{kT}\right) \sinh\left(\frac{V \cdot \beta \cdot ez \cdot a}{2kT}\right), \tag{11}$$

where β is the electric field fitting parameter with units of cm^{-1}. In the on-state, the filament radius after a time step, dt, is given by

$$r_{n+1} = r_n \sqrt{\frac{dt \cdot j_{hop-on}}{LzqN_{Ag}} + 1}, \tag{12}$$

where r_{n+1} is the radius after dt, and r_n is the radius before dt. The model assumes an initial radius of 2 nm. Once the filament bridges, the radius quickly grows until the resistance is reduced to where the current becomes limited and the voltage drops below the threshold for electrodeposition. A larger current limit allows the resistance to drop lower since the threshold for electrodeposition is fixed. This is why the ON resistance varies inversely with the compliance current limit.

The parameters used in the filament growth Eqs.6-12 and the electro-deposition/dissolution thresholds are reported in Table 12.

Table 12: Parameters for filament growth

Parameter	Value	Unit	Description
k	$8.617x10^{-5}$	eV/K	Boltzmann constant
ze	$1.602x10^{-19}$	C	Charge per ion
$2zeca\omega$	$5.379x10^{-3}$	A/cm^2	Mott-Gurney lumped coefficient
a	$6x10^{-8}$	cm	Effective hopping distance
W_{a-fwd}	0.310	eV	Forward hopping activation energy
W_{a-rev}	0.206	eV	Reverse hopping activation energy
T_0	295	K	Equilibrium temperature
R_{th}	$1.0x10^{-5}$	K/W	Thermal resistance
N_A	$6.022x10^{-23}$	mol^{-1}	Avogadro constant
ρ_{Ag_2Se}	8.216	g/cm^3	Ag_2Se density
m_{Ag_2Se}	294.7	g/mol	Ag_2Se molar mass
N_{Ag}	$3.358x10^{22}$	cm^{-3}	Ag concentration in filament
β	0.6	cm^{-1}	E-field fitting parameter
V_{fwd}	0.1	V	Electrodeposition threshold
V_{rev}	-0.05	V	Electrodissolution threshold

4.9 Compliance Current Implementation

Compliance current is the maximum allowable electrical current to a device under test. The Agilent 4156C has a compliance current setting to limit the current supplied to the device under test. A PMC is usually tested with compliance current to prevent overheating and to set different values of resistance. That same type of current limiting is needed in the numerical model so the same tests can be simulated. Current is limited by reducing the applied voltage. In the numerical model, the voltage is constant during each time step. The model performs compliance checks and adjustments at the beginning and end of each time step. If the current exceeds compliance at the beginning of the step, then the reduced voltage is calculated to yield compliance by

$$V = I_{comp} \cdot R \cdot sgn(V_{in}), \tag{13}$$

where I_{comp} is the compliance current and V_{in} is the unadjusted input voltage used to get the sign of the voltage. The filament can grow during the time step thereby decreasing the resistance and possibly causing the current to exceed the limit by the end of the step. Therefore, the current cannot be maintained exactly at the limit. A tolerance of 1% of the compliance current is allowed in the model. If the current exceeds compliance plus tolerance at the end of the step, then the time step, dt, is halved until the current remains in compliance at the end of the step.

4.10 Results

The quality of the simulation is shown in Figs. 37 and 38.

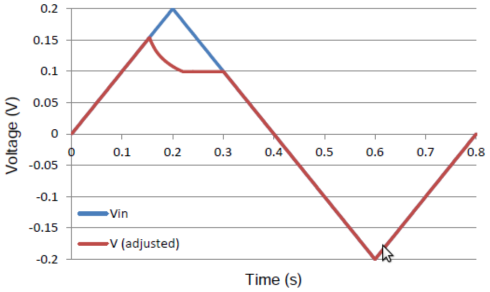

Figure 37: Simulated voltage input. Blue: user defined Red: Compiance-adjusted

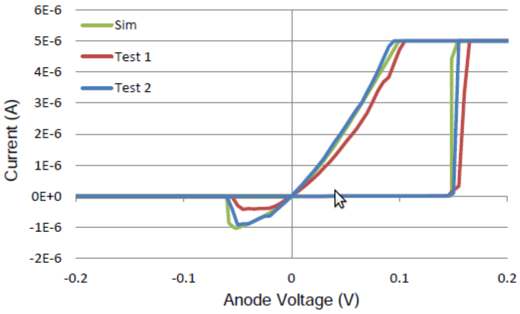

(a)

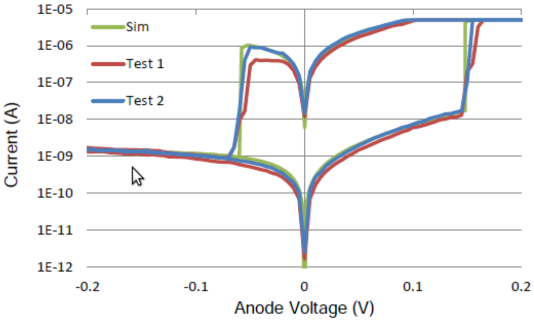

(b)

Figure 38: Simulated (green) and measured (red, blue) linear (a) logarithmic (b) I-V curves

Fig. 37 shows how the current-compliance constraint effects the actual applied voltage across the device. Figs. 38 show the excellent agreement, for both linear and logarithmic I-V curves obtained by this model. In Fig. 39, we show the R-V curves, comparing simulation and measurement.

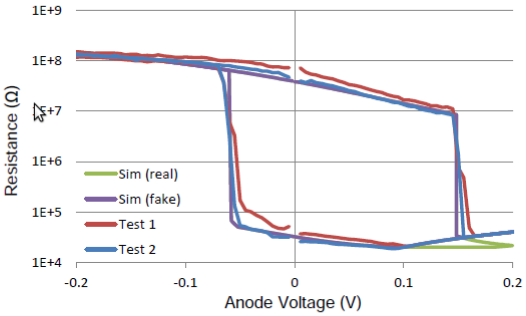

Figure 39: Simulated (green purple) and measured (red, blue) R-V curves

Note that there are two simulations, in green and purple, in Fig. 39. The purple calculates the resistance as the calculated current divided by the nominal input voltage that is shown in the purely triangular voltage (blue) in Fig. 37. This is, in fact, how the measurement equipment makes the calculation. The green reflects the actual resistance calculated from the current divided by the compliance-adjusted voltage.

4.11 Device Modeling: Kinetic Monte Carlo

Classical or quantum molecular dynamic (MD)s is often used to simulate time-dependent physics in solids. Using classical MD, one can include tens of thousands of atoms, and and follow system trajectories over ~ microseconds. The limitation on the time scale arises because the time step must be ~10^{-15}secs. to capture vibrations faithfully. The kinetic Monte Carlo technique (KMC) allows the inclusion of atomistic results, such as activation energies, and attempt-to-escape frequencies into a mesoscopic tool that allows for simulations on much larger time scales, because event probabilities are included in the method *a prioi.* We sample the probabilities of events randomly. This allows for improbable events to occur naturally, but on a much shorter simulation (wall clock) time scale. For a lucid discussion of the method, see Ref. [39]. We have, in fact, built our own simple KMC program based on Ref. [39] for a two dimensional lattice of sites. The physical system is modelled as in Fig. 40. Note that this is a stoichiometrically correct model, as each selenium is surrounded by two germanium atoms, and each germanium atom is surrounded by three selenium atoms and one germanium atom. $GeSe_2$could be modeled simply by placing selenium atoms between nearest-neighbor germanium atoms. In fact, we could do this randomly to simulate any x in $Ge_{1-x}Se_x$. We simply associate different parameters with each kind of site.

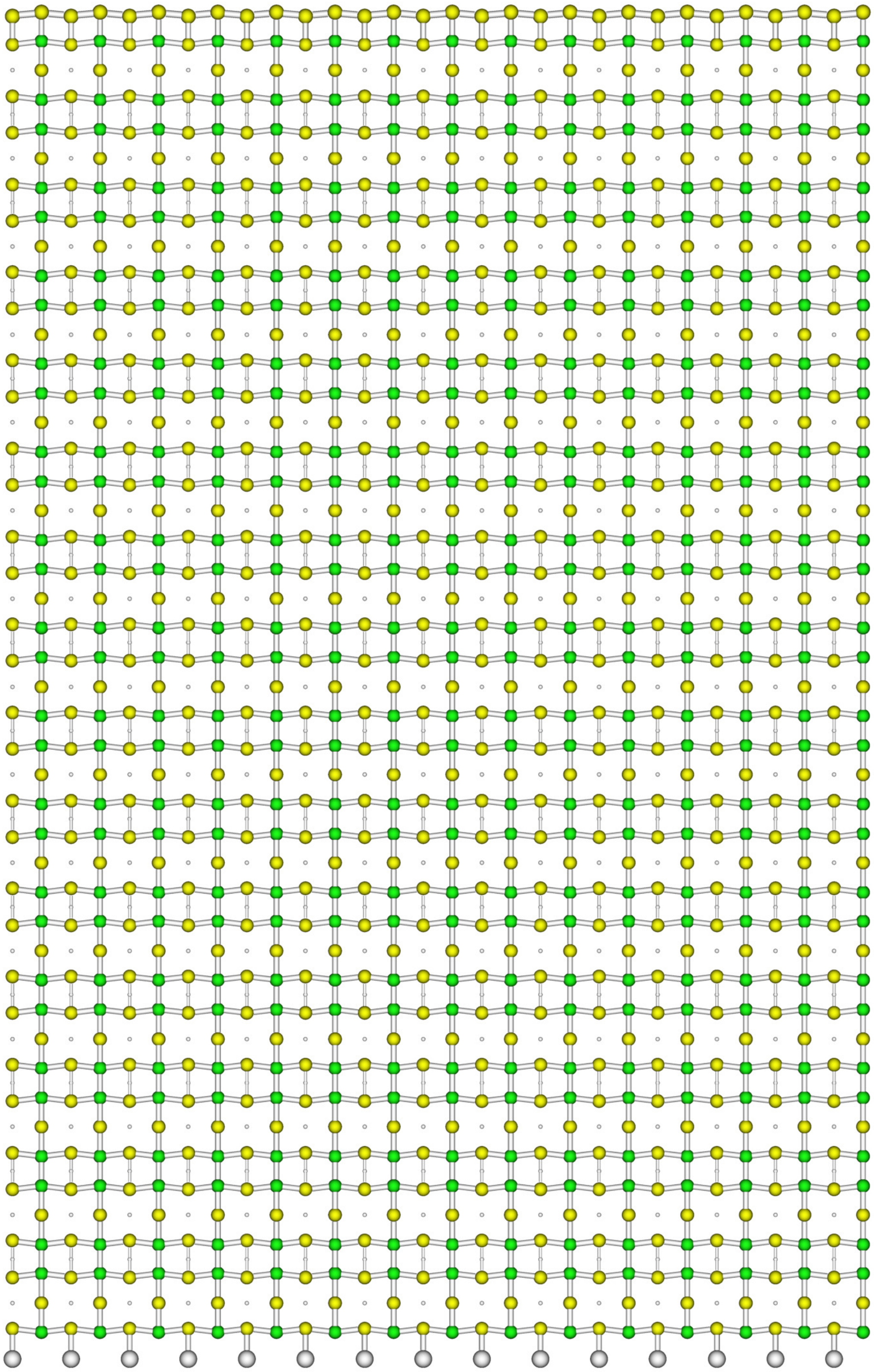

Figure 40: Model 2-d Ge_2Se_3 Green Ge, yellow Se (interior) or W (top boundary), and silver Ag

To date, we have demonstrated that our code is valid by simulating interstitial diffusion, and comparing this to the macroscopic diffusion equation. The results are shown in Fig. 41,

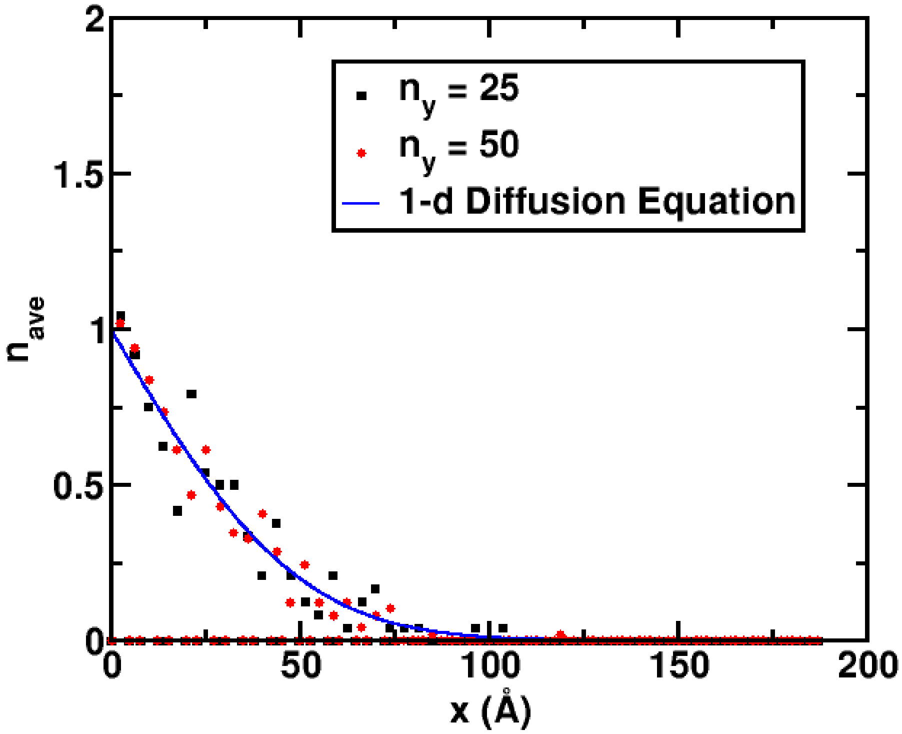

Figure 41: Comparison between macroscopic diffusion equation and KMC

To obtain this result, we assumed the same activation energy and attempt to escape frequency for the diffusion coefficient and for the KMC hopping probability. We assumed an infinite silver source and identical activation energy for silver entering Ge_2Se_3as for hopping between interstitial sites. The zeroes merely indicate that there are no silver atoms substituting on lattice sites initially occupied by either selenium or germanium. We simply did not include this process in the simulation. The value $n_{ave}$is simply the fractional occupation for a given row of sites. We varied the width of the device from 25 to 50 sites. Note that the wider device has tighter agreement with the analytical value.

The last improvement we implemented was to include a bias term. We did this by assuming the distance between hopping sites was 4 Å, and the activation was biased by the applied field times the hopping distance. The results are shown n Fig. 42.

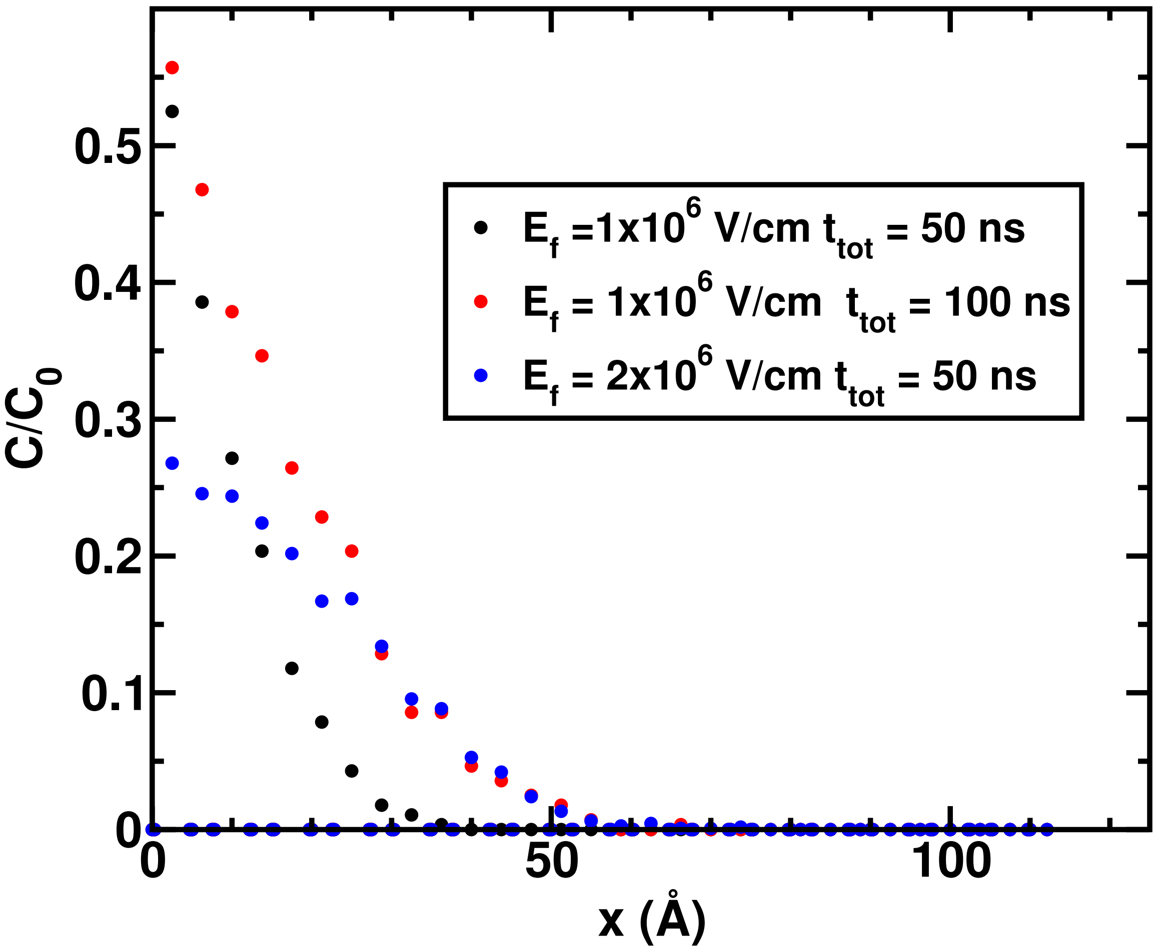

Figure 42: Bias dependent silver diffusion in KMC-model Ge_2Se_3

These are room temperature results. Note that the initial value within the material is below unity because we have no bias dependence on the initial hop into the material. We have no analytical solution to compare to. We only note that the qualitative results are reasonable– either longer time at the same bias or increased bias at the same time leds to the greater dirft-diffusion. That the increased electric field leads to a smaller value at the silver interface merely reflects that the silver is diffusing away faster than it is being supplied, and the the greater the bias, the greater the discrepancy between supply and diffusion.

5.0 FUTURE WORK

The work on oxygen seems to have a fairly clear exit. The work on single oxygen is tantalizingly close to conclusion. To be complete, we need to finish the work on Ge-O-Ge$_\perp$, and on the single hop between two Ge-O-Se-Ge sites. We should then have a complete picture of oxygen atom motion in chemically ordered, stoichiometric Ge_2Se_3. We need to do the kinetics of oxygen molecule dissociation. We have prejudices about how this will go and we are keen to see how well these agree with calculations. We are also keen to make some specific experimental predictions. Finally, we will be applying the same analysis to $GeSe_2$. The main question will be how transferable are the Ge-O-Se-Ge results when a germanium atom has four selenium nearest-neighbors. Of particular interest is the question of silver clustering in Ge_2Se_3. While we have some results on pairs of silver atoms, including that forming Ag dimers is thermodynamically favorable, work on larger clusters would be very interesting. Also, pursuing the role of tin, especially the kinetics of Ag-Sn dimer formation, could be revealing on a very practical level. The work on kinetic Monte Carlo is probably the most incomplete. We have a working KMC code, including field-induced drift, and we have some of the required parameters to study fully silver transport. This work would integrate many or our static results and could give deep insight into dendrite formation.

6.0 CONCLUSIONS

In this effort we have uncovered fundamental physical processes in pure Ge_2Se_3, in the Ge_2Se_3:Ag material system, and in the simplest conductive silver systems. In pure Ge_2Se_3, we have predicted that electrons will self-trap in pairs, causing significant disruptions of the continuous random network. We have also predicted that at low temperature, single self-trapped electrons should be observable, and that they should have observable spin-resonance signatures. We have calculated transport properties for both the single and paired self-trapped electrons, and find that self-trapped electrons have very low mobility, that transit times across a micron-sized sample would take seconds. The recognition of self-trapping in pure Ge_2Se_3 is crucial to understanding the physics of silver incorporation. We found that, because the atomic *5s* state is above the Ge_2Se_3 conduction band edge, interstitial silver autoioinizes, dropping an electron into the conduction band. We anticipate these mobile electrons will self-trap, as observed in our calculations. This complicates the interpretation of formation energies as a function of charge state for any defects that include interstitial silver. We have also shown that isolated silver prefers to be interstitial, although it costs very little energy (~0.1 eV) to transform to a silver substitutional and an interstitial germanium atom. We have also shown that silver readily pairs, either as interstitials or as substitutionals, and that the lowest energy configuration is a silver dimer substituting in a germanium dimer site. The addition of tin lowers further the reaction energies for silver incorporation. We have considered the emergence of metallic silver as a function of silver cluster size. We found that, for isolated silver clusters a ten atom cluster is sufficient to close the band gap– a prerequisite for metallic behavior. For both finite and infinite monomeric dendrites, silver is non-metallic. However, for dendrites with three atom-cross sections and above, infinite dendrites become metallic, although we have not yet calculated conductivities as a function of dendrite thickness.

We studied the interaction of oxygen with Ge_2Se_3. We found that oxygen will readily attack Ge-Ge dimers forming Ge-O-Ge bridges, and that this was an exothermic reaction. We found that silver would not attack these Ge-O-Ge bridges, and that oxygen would not readily break Ge-Ag dimers. The former implies that oxygenated Ge_2Se_3will not form silver dendrits the same way the the pure system would, so that it is important to keep oxygen out of the materials during fabrication. Oxygen substitutes readily for selenium with a formation energy of -1.6 eV, again, exothermic.

We have performed an initial study of copper and silver in SiO_2, and find that this is a fundamentally different system. We see no evidence for autoionization of either species. However, if the Fermi level is near mid-gap, we do predict that isolated copper and silver will be positively charged. Furthermore, we predict that copper will be singly charged, and not Cu^{2+}, as is often assumed. We found that in crystalline SiO_2, Cu^+will be highly mobile, with an activation energy less than 0.1 eV.

All of our results are for model crystalline systems. We should stress, however, that the physics articulated here will be present in any density functional calculation on stoichiometrically identical, and even similar, systems. The driver for autoionization in Ge-Se compounds is the size of the band gap, and the position of the atomic *5s* state state relative to the conduction band edge. These parameters will change little in larger quantum molecular dynamics studies. The physics will merely be buried in more complicated phenomena.

7.0 REFERENCES

REFERENCES

[1] N. A. Bakr, M. S. Aziz, and M. Hammam. Structural Properties of Ge_xSe_{1-x} Thin Films Prepared by Semi-closed Space Technique. *Egypt. J. Sol.*, 23(1):45–57, 2000.

[2] A. D. Becke. Density-functional thermochemistry. III. The role of exact exchange. *J. Chem. Phys*, 98(7):5648–52, April 1993.

[3] W. Chen, H. J. Barnaby, M. N. Kozicki, and A. H. Edwards. A Study of Gamma-Ray Exposure of Cu-SiO2 Programmable Metallization Cells . *IEEE Trans. Nuc. Sci.*, 62:2404–2411, 2015.

[4] W. Chen, S. Tappertzhofen, H. J. Barnaby, and M. N. Kozicki. SiO_2 based conductive bridging random access memory. 39:109–131, 2017.

[5] J. Choi, A. Singh, E. A. Davis, and S. J. Gurman. Optical properties and structure of unhydrogenated, hydrogenated, and zinc-alloyed a-Ge_xSe_{1-x} films prepared by radio-frequency sputtering. *J. Non-Cryst. Solids*, 198–200:680–683, 1996.

[6] M. Durandurdu and D. A. Drabold. Simulation of pressure-induced polyamorphism in a chalcogenide glass $GeSe_2$. *Phys. Rev. B*, 65:104208, 2002.

[7] A. H. Edwards, H. J. Barnaby, K. A. Campbell, M. N. Kozicki, W. Liu, and M. J. Marinella. Reconfigurable Memristive Device Technologies. *Proceedings of the IEEE*, 103(7):1004–1033, Jul 2015.

[8] A. H. Edwards, K. A. Campbell, and A. C. Pineda. Self-trapping of single and paired electrons in Ge_2Se_3. *J. Phys. Condens. Matter*, 24:195801, 2012.

[9] A. H. Edwards and W. B. Fowler. Theory of the peroxy-radical defect in a-SiO_2. *Phys. Rev. B*, 26:6649– 6660, 1982.

[10] T. Erdey-Grüz and M. Volmer. Zur Theorie der Wasserstoff Überspannung. *Z. Phys. Chem.*, 150 (A):203–213, 1930.

[11] P. H. Fuoss and A. Fischer-Colbrie. Structure of a -$GeSe_2$ from x-ray scattering measurements. *Phys. Rev. B*, 38:1875–1878, Jul 1988.

[12] D. R. Hamann. Generalized norm-conserving pseudopotentials. *Phys. Rev. B*, 40:2980–2987, 1989.

[13] Y. Hirose and H. Hirose. Polarity-dependent memory switching and behavior of Ag dendrite in Ag-photodoped amorphous As_2S_3 films . *J. Appl. Phys.*, 47:2767–2772, 1976.

[14] C. Huang and A. N. Cormack. The structure of sodium silicate glass. *J. Chem. Phys.*, 93:8180–8186, 1990.

[15] D. Ielmini. Filamentary-switching model in RRAM for time, energy and scaling projections. *IEDM Tech. Dig.*, 2011:17.2.1–17.2.4, 2011.

[16] H. Jonsson, G. Mills, and K. W.Jacobsen. *Classical and Quantum Dynamics in Condensed Phase Simulations*, page 385. World Scientific, Singapore, 1998.

[17] M. F. Kotkata, K. M. Kandil, and M. L. Théye. Optical studies of disorder and defects in amorphous Ge_xSe_{1-x} films as a function of composition. *J. Non-Cryst. Solids*, 164–166:1259–1262, 1993.

[18] M. C. S. Kumar and B. Pradeep. Electrical properties of silver selenide thin films prepared by reactive evaporation. *Bull. Mater. Sci.*, 25:407–411, 2002.

[19] S. Le Roux, A. Bouzid, M. Boero, and C. Massobrio. Structural properties of glassy Ge_2Se_3 from first-principles molecular dynamics. *Phys. Rev. B*, 86:224201, 2012.

[20] S. Le Roux, A. Zeidler, P. S. Salmon, M. Boero, M. Micoulaut, and C. Massobrio. Structural properties of liquid Ge_2Se_3 : A first-principles study. *Phys. Rev. B*, 84:134203, 2011.

[21] C. Massobrio, A. Pasquarello, and R. Car. Concentration Â¯uctuations on intermediate range distances in liquid $GeSe_2$: the critical role of ionicity. *Comp. Mat. Sci.*, 17:115–121, 2000.

[22] Carlo Massobrio, Alfredo Pasquarello, and Roberto Car. Microscopic Structure of Liquid $GeSe_2$: The Problem of Concentration Fluctuations over Intermediate Range Distances. *Phys. Rev. Lett.*, 80:2342–2345, Mar 1998.

[23] R. L. Meek. Diffusion Coefficient for Oxygen in Vitreous SiO_2. *J. Am. Ceram. Soc.*, 56:341–342, 1973.

[24] M. Mitkova, M. N. Kozicki, H. C. Kim, and T. L. Alford. Crystallization effects in annealed thin Ge–Se films photodiffused with Ag. *J. Non-Cryst. Solids*, 352:1986–1990, 2006.

[25] H. J. Monkhorst and J. D. Pack. Special points for Brillouin-zone integrations. *Phys. Rev. B*, 13:5188–92, 1976.

[26] N. F. Mott and R. W. Gurney. *Electronic Processes in Ionic Crystals*. Clarendon Press, 1948.

[27] P. Nachtigall, K. D. Jordan, A. Smith, and H. Jonsson. Investigation of the reliability of density functional methods: Reaction and activation energies for Si–Si bond cleavage and H2 elimination from silanes. *J. Chem. Phys*, 104(1):148–58, Jan 1996.

[28] J. Neugebauer and C. Van de Walle. Atomic geometry and electronic structure of native defects in GaN. *Phys. Rev. B.*, 50(11):8067–8070, 1994.

[29] F. J. Norton. Permeation of gaseous Oxygen through Vitreous Silica. *Nature*, 191:701, 1961.

[30] J. P. Perdew, K. Burke, and M. Ernzerhof. Generalized Gradient Approximation Made Simple. *Phys. Rev. Lett.*, 77(18):3865–3868, 1996.

[31] K. Ploog, W.Stetter, and A. Nowitzki. Crystal Growth and Structure Determination of Silicon Telluride Si_2Te_3. *Mater. Res. Bull. (USA)*, 11:1147–1154, 1976.

[32] M. Pohle, A. Feltz, H. Steil, and G. Herms. GLASS FORMATION AND PROPERTIES OF CHALCOGENIDE SYSTEMS XXXII. RDF studies on the structure of vitreous Ge_2S_3 and Ge_2Se_3. *J. Non-Cryst. Solids*, 69:283–91, 1985.

[33] Dirk Porezag and Mark R. Pederson. Optimization of Gaussian basis sets for density-functional calculations. *Phys. Rev. A*, 60(4):2840–2847, Oct 1999.

[34] J. Sarnthein, A. Pasquarello, and R. Car. Model of vitreous SiO_2 generated by an ab initio molecular-dynamics quench from the melt. *Phys. Rev B*, 52(17):12690–12695, 1995.

[35] M. W. Schmidt, K. K. Baldridge, J. A. Boatz, S. T. Elbert, M. S. Gordon, J. H. Jensen, S. Koseki, N. Natsunaga, K. A. Nguyen, S. J. Su, T. L. Windus, M. Dupuis, and J. A. Mongtomery. General Atomic and Molecular Electronic Structure System. *J. Comput. Chem.*, 14:1347–1363, 1993.

[36] W. J. Stevens, H. Basch, and M. Krauss. Effective Core Potentials for. *J. Chem. Phys.*, 81:6026–6033, 1984.

[37] T. P. Straatsma, E. Apra, T. L. Windus, E. J. Bylaska, W. de Jong, and S. Hirata. NWChem, A Computational Package for Parallel Computers, Version 4.6 (2004). Technical report, Pacific Northwest National Laboratory, 2004.

[38] R. M. Van Ginhoven, H. Jónsson, and L. R. Corrales. Silica glass structure generation for ab initio calculations using small samples of amorphous silica. *Phys. Rev B*, 71:024208, 2005.

[39] A. F. Voter. *INTRODUCTION TO THE KINETIC MONTE CARLO METHOD* , volume 235 of *NATO SCIENCE SERIES, SERIES II: MATHEMATICS, PHYSICS AND CHEMISTRY*, pages 1–23. Springer, Dordecht, 2007.

[40] W.J.Stevens, M.Krauss, H.Basch, and P.G.Jasien. . *Can.J.Chem.*, 70:612–630, 1992.

[41] Q. Yan, H. Jain, J. Ren, D. Zhao, and G. Chen. Effect of Photo-Oxidation on Photobleaching of $GeSe_2$ and Ge_2Se_3 Films. *J. Phys. Chem. C*, 115:21390–21395, 2011.

[42] S. Yu and H.-P. Wong. Compact Modeling of Conducting-Bridge Random-Access Memory (CBRAM). *IEEE Trans. Electron Devices*, 58:1352–1360, 2011.

[43] W. Zhou, M. Paesler, and D. E. Sayers. Structure of germanium-selenium glasses: An x-ray absorption fine-structure study. *Phys. Rev. B*, 43:2315–21, 1991.

GLOSSARY

1. **B3LYP** —Becke 3parameter Lee Yang Parr
2. **CB** —conduction band
3. **CBRAM** —conductive bridge random access memory
4. **ChG** —chalcogenide
5. **DFT** —density functional theory
6. **DZP** —double zeta plus polarization
7. **ECP** —exchange correlation potential
8. **ESR** —electron spin resonance
9. **EXAFS** —Extended X-ray absorption fine structure
10. **KMC** —Kinetic Monte Carlo
11. **PBE** —Perdew Burke Ernzerhoff
12. **PDOS** —Projected density of states
13. **PMC** —Programmable metallization Cell
14. **RT** —Room temperature
15. **STE** —self-trapped electron
16. **VB** —valence band

DISTRIBUTION LIST

DTIC/OCP 8725 John J. Kingman Rd, Suite 0944 Ft Belvoir, VA 22060-6218	1 cy
AFRL/RVIL Kirtland AFB, NM 87117-5776	1 cy
Official Record Copy AFRL/RVS/Arthur Edwards	1 cy